

# HCN/HNC intensity ratio: a new chemical thermometer for the molecular ISM ★

A. Hacar<sup>1</sup>, A. D. Bosman<sup>1</sup>, and E. F. van Dishoeck<sup>1</sup>

Leiden Observatory, Leiden University, P.O. Box 9513, 2300-RA Leiden, The Netherlands  
e-mail: hacar@strw.leidenuniv.nl

XXXX

## ABSTRACT

**Context.** The gas kinetic temperature ( $T_K$ ) determines the physical and chemical evolution of the Interstellar Medium (ISM). However, obtaining reliable  $T_K$  estimates usually requires expensive observations including the combination of multi-line analysis and dedicated radiative transfer calculations.

**Aims.** This work explores the use of HCN and HNC observations, and particularly its  $I(\text{HCN})/I(\text{HNC})$  intensity ratio of their  $J=1-0$  lines, as direct probe of the gas kinetic temperature in the molecular ISM.

**Methods.** We obtained a new set of large-scale observations of both HCN and HNC (1-0) lines along the Integral Shape Filament (ISF) in Orion. In combination with ancillary gas and dust temperature measurements, we find a systematic temperature dependence of the observed  $I(\text{HCN})/I(\text{HNC})$  intensity ratio across our maps. Additional comparisons with chemical models demonstrate that these observed  $I(\text{HCN})/I(\text{HNC})$  variations are driven by the effective destruction and isomerization mechanisms of HNC under low energy barriers.

**Results.** The observed variations of  $I(\text{HCN})/I(\text{HNC})$  with  $T_K$  can be described with a two-part linear function. This empirical calibration is then used to create a temperature map of the entire ISF. Comparisons with similar dust temperature measurements in this cloud, as well as in other regions and galactic surveys, validate this simple technique to obtain direct estimates of the gas kinetic temperature in a wide range of physical conditions and scales with an optimal working range between  $15 \text{ K} \lesssim T_K \leq 40 \text{ K}$ .

**Conclusions.** Both observations and models demonstrate the strong sensitivity of the  $I(\text{HCN})/I(\text{HNC})$  ratio to the gas kinetic temperature. Since these lines are easily obtained in observations of local and extragalactic sources, our results highlight the potential use of this observable as new chemical thermometer for the ISM.

**Key words.** ISM: clouds – ISM: molecules – ISM: structure – Stars: formation – Submillimeter: ISM

## 1. Introduction

The gas kinetic temperature ( $T_K$ ) represents the most fundamental thermodynamical property of the Interstellar Medium (ISM). In combination with the gas density  $n(\text{H}_2)$ , the value of  $T_K$  determines the gas pressure ( $P/k=n(\text{H}_2)T_K$ ) and thus the thermal support against gravity.  $T_K$  also sets the sound speed ( $c_s = \sqrt{(k T_K)/\mu}$ ) and the transition between both sonic and supersonic regimes. As a result,  $T_K$  sets the fragmentation scale of the star-forming gas in molecular clouds (Larson 1985). Moreover, the gas kinetic temperature regulates the chemical properties of the molecular gas defining the activation and rate of gas-phase reactions (van Dishoeck 2018). Observationally,  $T_K$  also influences the excitation conditions and intensities of both atomic and molecular emission lines (e.g., Shirley 2015). Obtaining accurate and systematic measurements of  $T_K$  is therefore a key ingredient to describe the physical and chemical evolution of the ISM.

Different observational methods have been classically employed to estimate the gas kinetic temperature in the molecular ISM using line and continuum observations.  $T_K$  is regularly estimated from the analysis of the excitation temperatures ( $T_{\text{ex}}$ ) and level populations (Goldsmith & Langer 1999)

using multiple transitions of the same tracer such as CO-ladders (e.g., Peng et al. 2012). Similarly,  $T_K$  can be evaluated using temperature-sensitive transitions of either single tracers (e.g.,  $\text{H}_2\text{CO}$ ; Mangum, & Wootten 1993; Ginsburg et al. 2016) or multiple isotopologues (e.g.,  $^{12}\text{CO}$ ,  $^{13}\text{CO}$ , and  $\text{C}^{18}\text{O}$ ; Nishimura et al. 2015) in combination with radiative transfer models (e.g., large velocity gradients, LVG). The gas kinetic temperature can also be inferred from the rotational temperatures ( $T_{\text{rot}}$ ) of collisionally excited transitions of density selective tracers such as  $\text{NH}_3$  (Ho & Townes 1983). On the other hand, recent FIR space observatories (i.e., *Herschel* and *Planck*) have popularized the use of dust temperature estimates ( $T_{\text{dust}}$ ) as a proxy of  $T_K$  using multiwavelength continuum observations (e.g., Lombardi et al. 2014).

Thanks to the recent development of broad-band heterodyne receivers, spectral molecular maps with hundreds or thousands of individual beams are nowadays routinely produced in all kinds of ISM studies of protoplanetary disks (Jørgensen et al. 2016), molecular clouds (Pety et al. 2017), and nearby galaxies (Jiménez-Donaire et al. 2019) using radiotelescopes such as the IRAM30m or the Atacama Large Millimeter Array (ALMA). While created for the study of individual sources, the use the above temperature estimates in these large molecular datasets is nevertheless far from trivial. Obtaining  $T_K$  estimates in massive molecular datasets usually requires expensive observations of multiple transitions at different frequencies

★ Based on observations carried out with the IRAM30m Telescope. IRAM is supported by INSU/CNRS (France), MPG (Germany) and IGN (Spain).

(e.g., CO-ladders) and complex fitting procedures of thousand of spectra (e.g.,  $\text{NH}_3$ ). In most cases, this analysis is also complicated by the necessary combination with complex chemical and radiative transfer calculations in order to evaluate observational biases such as opacity, excitation, and line-of-sight effects. Moreover, the application of many of these methods requires the underlying assumption of Local Thermodynamic Equilibrium (LTE;  $T_K = T_{\text{ex}} \sim T_{\text{rot}}$ ) and/or an effective dust-to-gas coupling ( $T_K = T_{\text{dust}}$ ), properties that are not necessary satisfied under most of the ISM conditions (e.g., Goldsmith 2001). These observational biases have usually limited the application of these techniques to some dedicated studies. On the contrary, the detailed description of the temperature structure of the gas in molecular clouds remains largely unconstrained.

Following one of the long-standing debates in astrochemistry (e.g., Herbst et al. 2000), this paper explores the use of the HCN/HNC line ratio as a new chemical thermometer of the molecular ISM. The favourable observational conditions and widespread detection of both HCN (cyanide) and HNC (isocyanide) isomers make this observable a potential direct probe of the gas temperature within a wide range of scales and densities in the ISM. Using a new set of large-scale IRAM30m observations in the Orion A cloud (Sect. 2), we compare in this work the observed variations of the  $I(\text{HCN})/I(\text{HNC})$  intensity ratio of the  $J=1-0$  lines with both independent temperature estimates and chemical models (Sect. 3). Our observational and model results demonstrate the strong sensitivity and systematic dependence of this  $I(\text{HCN})/I(\text{HNC})$  ratio with the gas kinetic temperature  $T_K$  between  $\sim 10$  and  $50$  K. We calibrate this empirical correlation (Sect. 4) in order to obtain a large-scale temperature map of the Orion A cloud (Sect. 4.2). Applied to other star-forming regions and galactic surveys, our temperatures estimates show an excellent correlation with independent dust temperature measurements in a wide range of ISM environments within an optimal range between  $10$  and  $40$  K (Sect. 4.4). Driven by the effective destruction of HNC, plus its isomerization into HCN, this temperature dependence could potentially explain the enhanced  $I(\text{HCN})$  intensities observed in star-forming galaxies (Sect. 5.2).

## 2. Large-scale IRAM30m observations in Orion

We systematically investigated the emission of the ground ( $J=1-0$ ) transitions of both HCN ( $\nu = 88.631$  GHz, CDMS; Müller et al. 2001) and HNC ( $\nu = 90.663$  MHz, CDMS; Müller et al. 2001) isotopomers along the Integral Shape Filament (ISF) in Orion (Bally et al. 1987) using a new set of large-scale IRAM30m molecular maps<sup>1</sup>. Our observations follow the main spine of this massive filament delineated in the dust continuum (Johnstone & Bally 1999; Lombardi et al. 2014) and dense tracers such as  $\text{NH}_3$  (Friesen et al. 2017) and  $\text{N}_2\text{H}^+$  (Tatematsu et al. 2008; Hacar et al. 2017a). As illustrated in Fig.1, our observations cover a total area of  $1.1 \times 0.14$  deg<sup>2</sup> in size, that is,  $\sim 8 \times 1$  pc<sup>2</sup> at distance of  $414$  pc (Menten et al. 2007), including the OMC 1-4S clouds, the entire Orion Nebula Cluster (ONC), the West half of the M43 nebula, as well as the Southernmost end of the NGC 1977 cluster (see Peterson & Megeath 2008, for a description of these regions).

The bulk of our IRAM30m observations correspond to the central part of the ISF extending along the OMC 1-4 clouds (proj.ID: 032-13), already presented by Hacar et al. (2017a). To-

gether with the  $\text{N}_2\text{H}^+$  ( $1-0$ ) line previously surveyed at high velocity resolution, we simultaneously observed both HCN ( $1-0$ ) and HNC ( $1-0$ ) lines using the EMIR receiver connected to the FTS backend configured to a fine spectral resolution of  $195$  kHz, corresponding to  $\sim 0.7$  km s<sup>-1</sup> at the frequency of these lines. In order to produce a large-scale mosaic, we combined different Nyquist-sampled On-The-Fly (OTF) maps, typically of  $200 \times 200$  arcsec<sup>2</sup> each, observed in Position-Switching (PSw) mode. Following standard procedures, we carried out atmospheric calibration every  $15$  min, as well as focus and pointing corrections every  $1.5-2$  hours. Three distinct positions along the cloud were systematically observed every  $2$  hours as reference spectra for cross calibration between different runs (see Hacar et al. 2017a, for additional information).

We complemented our previous large-scale maps with additional observations of the OMC-4 South (OMC-4S) region (proj.ID: 034-16) carried out between August and November of 2016 under average summer conditions with PWV=5mm. We used a spectroscopic EMIR + FTS setup and mapping strategy similar to our previous observing campaign, this time in Frequency Switching mode (FSw). In addition to the corresponding standard pointing and focus measurements, the same reference spectra already sampled in PSw mode along OMC-1 were re-observed in FSw mode finding consistent intensities within the  $\sim 15\%$  calibration uncertainties of the telescope.

An additional EMIR sideband was connected to an extra FTS unit in order to simultaneously survey the  $\text{H}41\alpha$  recombination line ( $\nu = 92.034$  GHz). The central part of this dataset was presented by Goicoechea et al. (2015) for the analysis of the [CII] and molecular emissions in the ONC. Similar to our previous molecular dataset, our last observing campaign extended these observations toward the OMC-4S region creating a large mosaic of the entire ISF.

All of our IRAM30m observations were reduced using the GILDAS/CLASS software<sup>2</sup>. Each individual dataset, with native resolution of  $\sim 27''$ , was independently combined and convolved into a common Nyquist-sampled grid with a final resolution of  $30''$  with a total  $\sim 8950$  independent spectra for each of the lines in our survey. Given the large velocity variations observed within this cloud (e.g., Goicoechea et al. 2015; Hacar et al. 2017a), we applied local baseline corrections to each individual spectrum adapting each line window according to the specific target line and position in our maps. We converted the observed line intensities, originally in antenna temperature units, into main beam temperature units using facility provided efficiencies<sup>3</sup>. Finally, we obtain total integrated emission maps (i.e.,  $I(A) = \int T_{mb}(A) dv$ , in units of K km s<sup>-1</sup>) between  $[-20, 20]$  km s<sup>-1</sup> for the HCN ( $1-0$ ) (aka including all hyperfine components),  $[-10, 15]$  km s<sup>-1</sup> for HNC ( $1-0$ ) transitions, and between  $[-25, 20]$  km s<sup>-1</sup> for the  $\text{H}41\alpha$ . The above integration limits for HCN and HNC aim to capture the line intensities originating at the cloud velocities. The choice of this velocity range deliberately excludes the emission of the high velocity wings in the Orion BN/KL region. Therefore, the line intensities in this particular area should be considered as lower limits<sup>4</sup>.

<sup>2</sup> <http://www.iram.fr/IRAMFR/GILDAS>

<sup>3</sup> <http://www.iram.es/IRAMES/mainWiki/Iram30mEfficiencies>

<sup>4</sup> The integrated intensity maps for the HCN ( $1-0$ ), HNC ( $1-0$ ), and  $\text{H}41\alpha$  lines presented in Figure 1 will be available via CDS.

<sup>1</sup> This work is part of the ORION-4D project (PI: A. Hacar). See more information in <https://sites.google.com/site/orion4dproject>.

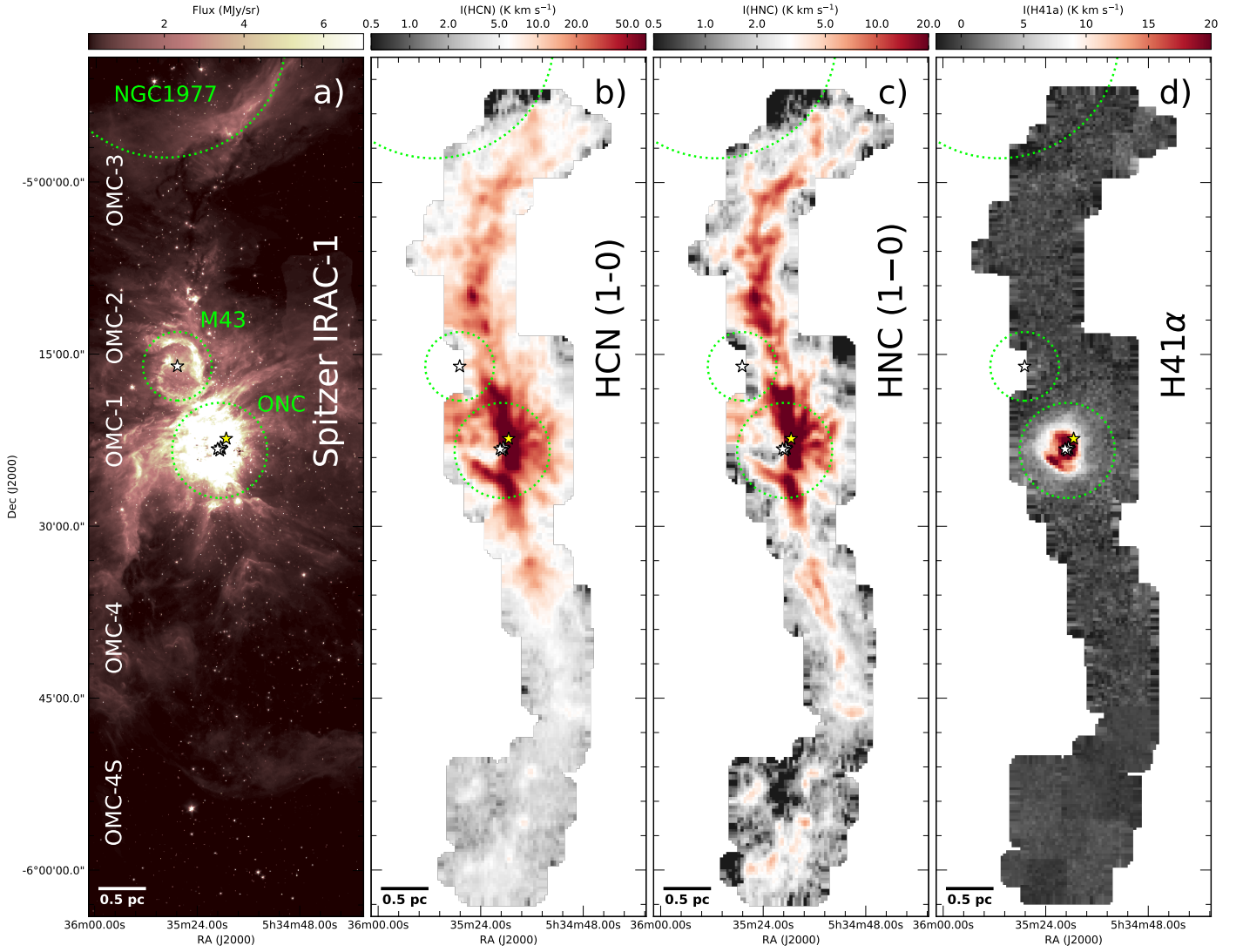


**Fig. 1.** New IRAM30m observations along the Orion ISF. From left to right: **(a)** Spitzer IRAC-1 emission map (Megeath et al. 2012); **(b)** HCN ( $J=1-0$ ), **(c)** HNC ( $J=1-0$ ), and **(d)** H41 $\alpha$  line intensity (aka total integrated intensity) maps (this work). We note that both HCN and HNC intensity maps are presented in logarithmic scales given the large dynamic range in emission showed by these two species. The different OMC 1-4 clouds, together with the different clusters and nebulosities, are indicated in the IRAC-1 image. For guidance, the extension of the ONC, M43, and NGC1977 regions (green dotted circles), as well the position of the Trapezium and NU Ori stars (white stars) plus the Orion BN source (yellow star), are also indicated in the different IRAM30m maps.

### 3. Results

#### 3.1. Observational correlation between HCN/HNC line ratio and the gas kinetic temperature

We present the HCN and HNC ( $J=1-0$ ) total integrated intensity maps (including all hyperfine components) along the ISF in Fig.1. As illustrated in panels (b-d), the emission maxima of these two species correspond with the central part of the ONC traced by H41 $\alpha$  emission showing extended regions with integrated intensities above  $I(\text{HCN}) \geq 50 \text{ K km s}^{-1}$  and  $I(\text{HNC}) \geq 20 \text{ K km s}^{-1}$ , respectively. Clearly recognized at the centre of our images, the emission of both HCN and HNC isotopomers highlights most of the well-known OMC-1 molecular fingers (e.g., Martin-Pintado et al. 1990) as well as the Orion bar (e.g., Tielens et al. 1993), seen in high contrast respect to their local environment. Prominent emission in these two lines, with  $I(\text{HCN}), I(\text{HNC}) > 10 \text{ K km s}^{-1}$ , also traces the northern part of the ISF towards the OMC-2 and OMC-3 clouds, showing multiple local peaks coincident with the position of several FIR

sources within these regions (e.g., OMC-2 FIR-4). On the other hand, both HCN and HNC intensities progressively decrease below  $I(\text{HCN}), I(\text{HNC}) < 5 \text{ K km s}^{-1}$  towards the OMC-4 and OMC-4S clouds.

The bright emission detected in both HCN and HNC ( $J=1-0$ ) line maps reflects the large dynamic range of column densities traced by these two species. While largely varying in intensity, both transitions are systematically detected in the vast majority of the positions surveyed by our IRAM30m observations. In particular, most of our HCN (99%) and HNC (93%) spectra show intensities above  $I(\text{HCN}), I(\text{HNC}) \geq 1 \text{ K km s}^{-1}$ , that is,  $S/N > 3$  respect to the typical  $\sigma \sim 0.3 \text{ K}$  in our maps. Independent FIR *Herschel* measurements (Lombardi et al. 2014) indicate that the above detections extend down to equivalent gas column densities of  $A_V \sim 3 \text{ mag}$  within the limits of our molecular maps. Similar to previous observations of this region (Kauffmann et al. 2017), the above detection thresholds indicate the presence and strong sensitivity of these HCN and HNC species not only to the high

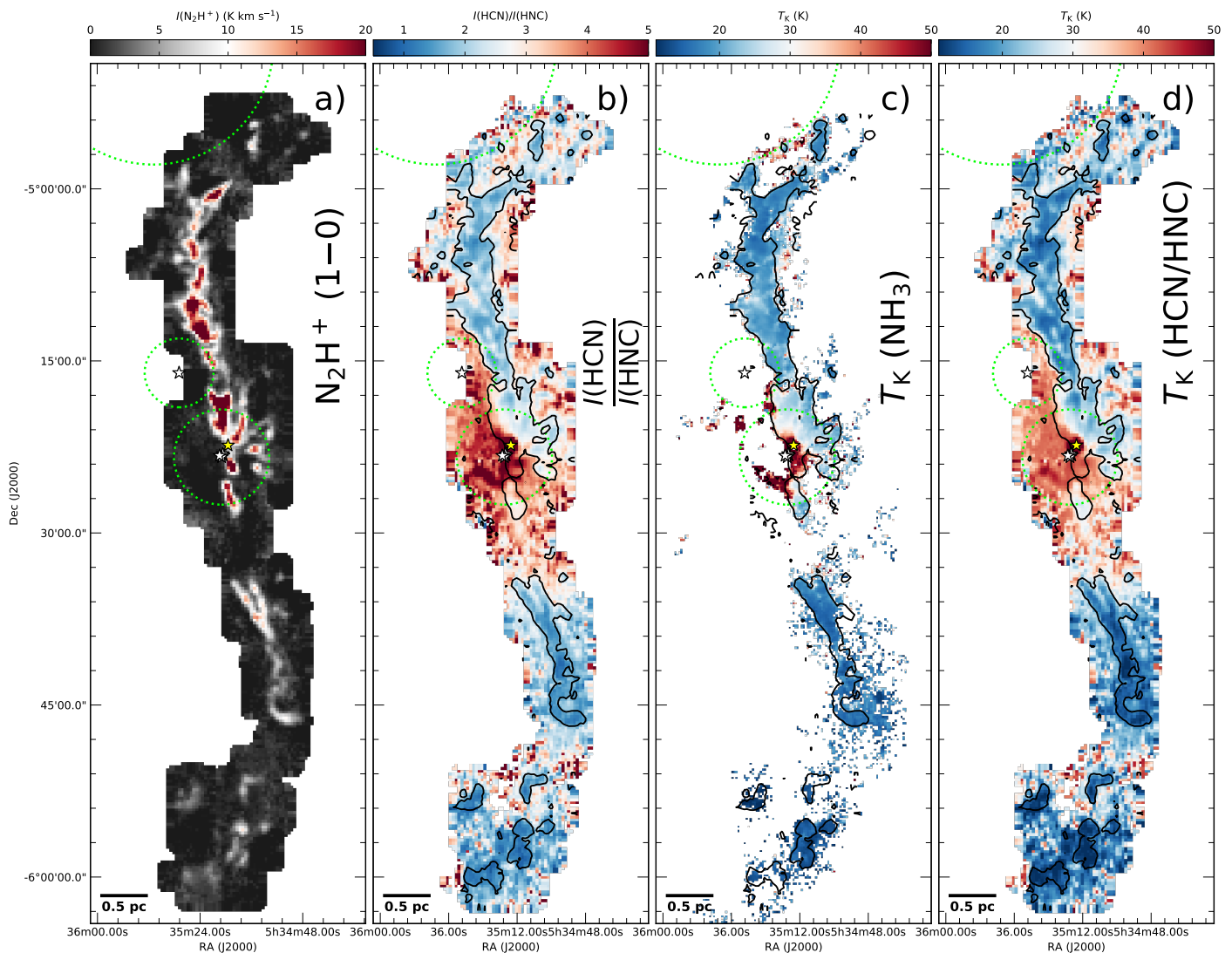


**Fig. 2.** From left to right: (a)  $\text{N}_2\text{H}^+$  (1-0) integrated emission (see also Hacar et al. 2017a), (b)  $I(\text{HCN})/I(\text{HNC})$  line intensity ratio (see also Fig. 1), (c) gas kinetic temperature map derived using  $\text{NH}_3$  measurements (Friesen et al. 2017), and (d) gas kinetic temperature map derived using the proposed  $I(\text{HCN})/I(\text{HNC})$  as temperature probe according to Eqs. 3 and 4 (this work). For comparison, we indicate the intensity contour with  $I(\text{N}_2\text{H}^+) = 1.5 \text{ K km s}^{-1}$  in panels (b-d). Circles and star symbols are similar to Fig. 1.

density gas but also to more extended and low column density material in this cloud (see also Pety et al. 2017).

While qualitatively similar in their overall distribution, we find large variations between the relative intensities of both HCN and HNC (1-0) transitions along the ISF. To illustrate this property, we present the total line intensity ratio  $I(\text{HCN})/I(\text{HNC})$  of these two lines in Fig. 2b. An eye inspection of this figure indicates that  $I(\text{HCN})/I(\text{HNC})$  varies more than an order of magnitude across the areas surveyed in our maps. In agreement with previous results (Goldsmith et al. 1986; Schilke et al. 1992; Ungerechts et al. 1997), the largest differences in emission are found in the surroundings of the Orion BN/KL region showing  $I(\text{HCN})/I(\text{HNC}) > 10$ . This line ratio decreases towards values of  $I(\text{HCN})/I(\text{HNC}) \sim 2 - 3$  in regions such OMC-2 and, more prominently, down to values of  $I(\text{HCN})/I(\text{HNC}) \sim 1$  in OMC-4.

In addition to these regional differences, we notice a systematic dependence of this  $I(\text{HCN})/I(\text{HNC})$  line ratio as function of column density. Particularly visible in the radial distribution of regions such as OMC-2, this reported line ratio varies from values of  $\sim 2 - 4$  at the cloud edges toward values close to unity at the centre of the ISF. Although less prominent in dynamic range,

a similar trend is also visible in regions like OMC-4 showing variations between  $\sim 3 - 1$ .

Interestingly, we find an excellent correspondence between the variations of the  $I(\text{HCN})/I(\text{HNC})$  line ratios in our ISF data and the gas kinetic temperatures ( $T_K$ ) using  $\text{NH}_3$  observations derived by the GBT-GAS survey (Friesen et al. 2017). As illustrated by the comparison of Fig. 2 b and Fig. 2 c, the lowest  $I(\text{HCN})/I(\text{HNC})$  ratios are typically found at the coldest regions at the centre of clouds like OMC-2 or OMC-4. Conversely, larger  $I(\text{HCN})/I(\text{HNC})$  values are shown at increasing gas temperatures both in regions such as OMC-1 and toward the cloud edges.

The above dependence between  $I(\text{HCN})/I(\text{HNC})$  and  $T_K$  becomes apparent in the point-to-point comparison displayed in Figure 3. There, we include all the positions surveyed in our maps showing  $I(\text{HCN})$ ,  $I(\text{HNC}) \geq 1 \text{ K km s}^{-1}$  and temperature estimates better than 50%, that is,  $(\delta T_K/T_K) \leq 0.5$ , according to Friesen et al. (2017) (grey crosses). As global trend, we identify a systematic increase of the  $I(\text{HCN})/I(\text{HNC})$  line ratio as function of temperature across the entire ISF, ranging from about  $L(\text{HCN})/L(\text{HNC}) \sim 1$  at  $T_K \leq 15 \text{ K}$  to  $L(\text{HCN})/L(\text{HNC}) \geq 5$

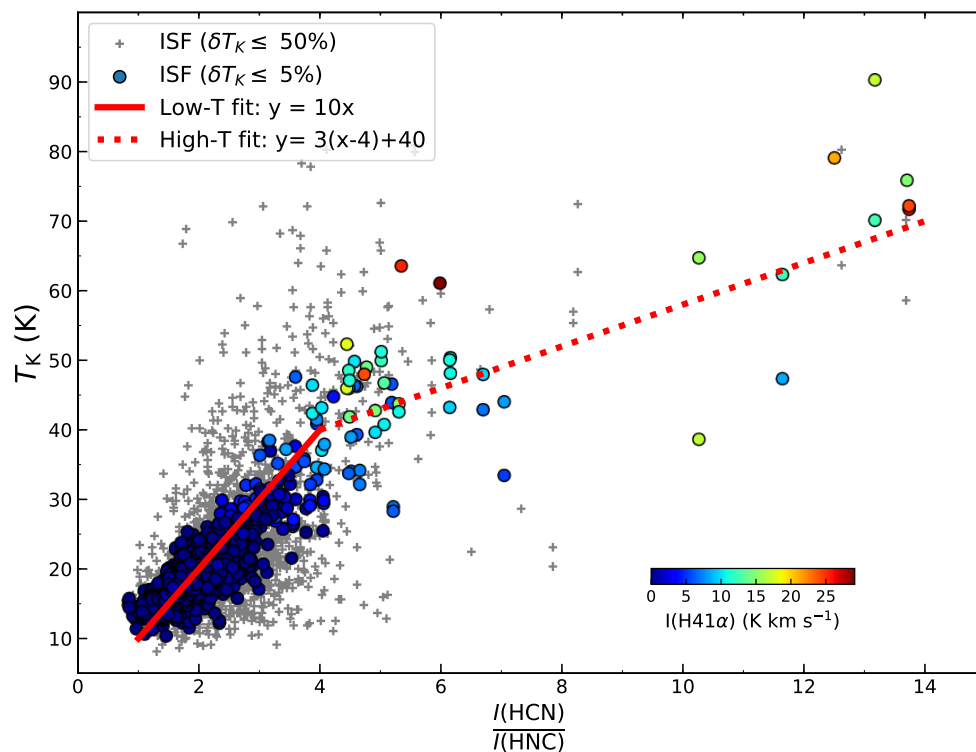


**Fig. 3.** Correlation between the observed  $I(\text{HCN})/I(\text{HNC})$  line ratios (this work) and measurements of the gas kinetic temperatures derived using  $\text{NH}_3$  observations (Friesen et al. 2017) with reliable temperature estimates (i.e.,  $\delta T_K/T_K \leq 50\%$ ; grey crosses). These positions with good temperature estimates (i.e.,  $\delta T_K/T_K \leq 5\%$ ) are colour coded according to their total  $\text{H}41\alpha$  intensity (see Fig. 1). A systematic increase of the gas kinetic temperatures in Orion is clearly visible in those positions with strong  $I(\text{H}41\alpha)$  emission denoting their proximity to the ONC. The empirical linear fit of both low- (solid red line) and high- (dotted red line) temperature regimes are indicated in the plot (see Sect. 4).

at  $T_K \geq 40$  K. The distribution of these points indicates a typical dispersion of about  $\pm 5$  K respect to this average behaviour. The use of only those positions with high quality temperature estimates, namely, better than 5% (or  $(\delta T_K/T_K) \leq 0.05$ ) (blue solid points), significantly reduces this scatter suggesting that a large fraction of this latter dispersion may be produced by the uncertainties associated with these previous temperature measurements.

### 3.2. Enhanced HCN/HNC abundance ratios at high gas temperatures

The systematic variation of the HCN and HNC intensity ratio as function of the gas kinetic temperature shown in Sect. 3.1 suggests a direct connection between the emission and thermal properties of the gas within the ISF. A priori, the variations of the observed line ratios can potentially originate from the distinct excitation, opacity, and abundance of these two isomers. In this section we examine which of these mechanisms are responsible of the observed  $I(\text{HCN})/I(\text{HNC})$  variations.

Since the abundance of HCN is generally larger than that of HNC in regions like the ONC (e.g., Goldsmith et al. 1981), the reported variations in the  $I(\text{HCN})/I(\text{HNC})$  measurements can potentially be explained by an increase of the HCN (1-0) line opacity. Theoretical and observational results indicate an inverse correlation between the observed cloud temperatures as function of the cloud depth. If the HNC (1-0) line remained optically thin, the saturation of the HCN (1-0) line would then reduce the observed  $I(\text{HCN})/I(\text{HNC})$  ratio in regions of increasing column densities and, therefore, decreasing temperatures. We measured the HCN (1-0) opacities from the analysis of the hyper-

fine structure of all the spectra in our maps. Assuming a single line component, we fitted each individual spectrum in our survey using the *hfs* method in CLASS assuming the hyperfine frequencies and relative intensities provided by the JPL database (Pickett et al. 1998)<sup>5</sup>. A total of 7810 HCN ( $J = 1-0$ ) spectra were fitted with  $S/N \geq 3$ . Among them, 83% are found to be optically thin, showing opacities of their central hyperfine component with  $\tau(F = 2-1) \leq 1$ . Those optically thick spectra, 98% of which show  $\tau(F = 2-1) = 1-3$ , are primarily concentrated in high column density areas within the OMC-4 and OMC-4S clouds. In contrast, most of the OMC-1, OMC-2, and OMC-3 spectra are found to be optically thin with opacities as low as  $\tau(F = 2-1) \leq 0.1$ . Nonetheless, we find hyperfine anomalies (Walmsley et al. 1982) in many of our HCN spectra around the ONC making their opacity estimates uncertain. In the absence of additional measurements (e.g.,  $\text{H}^{13}\text{CN}$ ), radiative transfer calculations using RADEX (van der Tak et al. 2007) demonstrate that the expected opacity variations can be responsible for changes of the  $I(\text{HCN})/I(\text{HNC})$  line ratios up to a factor of  $\sim 3$  (see also Appendix A). While likely affecting some spectra in our maps, these estimates allow us to rule out opacity as the main driver of

<sup>5</sup> For simplicity, we fitted all our spectra using a single-line component along the entire ISF. This assumption deliberately ignores the presence of more a complex kinematic substructure observed at interferometric resolutions in regions like OMC-1 and OMC-2 (Hacar et al. 2018). Previous single-dish studies indicate that most of this complexity is smoothed out at the resolution of our IRAM30m observations (Hacar et al. 2017a) potentially affecting our opacity estimates. These resolution effects are assumed to have a minor statistical impact in our large-scale analysis. Nevertheless, these caveats should be considered on the interpretation of individual spectra.



the global variations in the  $I(\text{HCN})/I(\text{HNC})$  line ratio observed along the ISF.

With minor opacity effects, the similar frequencies, dipole moments, and excitation conditions of both HCN and HNC (1-0) transitions make their intensity ratio a good proxy of the relative column densities of these two species (Goldsmith et al. 1986). In this sense, the results obtained in Sect. 2 would suggest a systematic variation of the relative abundances of the HCN and HNC molecules with respect to the gas kinetic temperature. We have quantified these abundance variations using RADEX. A series of simple tests with constant  $X(\text{HCN})$  and  $X(\text{HNC})$  abundances confirm the weak dependence of the observed  $I(\text{HCN})/I(\text{HNC})$  values as function of temperature (with changes of a factor  $\leq 2$ ) for a given isomer ratio. The observed variation ratios also exceed the uncertainties produced by the different collisional rate coefficients between HCN and HNC ( $\sim 5$  at low temperatures, Hernández Vera et al. 2017). Instead, only large isomeric abundance differences, of more than an order of magnitude in relative abundance (i.e.,  $X(\text{HCN})/X(\text{HNC}) = 1 - 20$ ), are able to reproduce the observed variations of this line intensity ratio as function of  $T_K$  shown in Fig. 3.

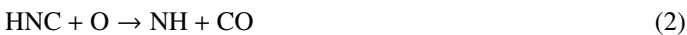
### 3.3. HNC destruction mechanisms: low energy barriers

Understanding the origin of the observed temperature dependence of the  $X(\text{HCN})/X(\text{HNC})$  abundance ratio in molecular clouds is an old question in astrochemistry studies (e.g., Wootten et al. 1978; Herbst et al. 2000). Large  $X(\text{HCN})/X(\text{HNC})$  abundance variations, by more than an order of magnitude, are regularly reported both within and between clouds as function of temperature (Goldsmith et al. 1981; Irvine & Schloerb 1984). Extreme ratios of  $X(\text{HCN})/X(\text{HNC}) > 30$  have traditionally been found at high temperatures in regions such as the ONC (Schilke et al. 1992). In contrast, much lower abundance ratios of  $X(\text{HCN})/X(\text{HNC}) \sim 0.7$  are typically observed in dense cores at lower temperatures (Harju 1989; Hirota et al. 1998). Compared to these previous results, the large dynamic range shown in Fig. 3 indicate a smooth connection between these warm and cold environments.

Different theoretical studies have suggested that the observed  $X(\text{HCN})/X(\text{HNC})$  variations could be chemically controlled. Laboratory experiments and chemical models agree upon the dissociative recombination of  $\text{HCNH}^+$  as the main the formation pathway of HCN and HNC molecules, forming both isomers with an approximately branching ratio of 1:1 at  $T_K < 200$  K (e.g., Herbst et al. 2000). With the same initial abundances, the observed isomer variations are therefore regulated by their destruction mechanisms. In particular, two neutral-neutral reactions have been proposed to be responsible of the observed temperature variations of the  $X(\text{HCN})/X(\text{HNC})$  abundance ratios in the ISM:



and



Classical ab-initio calculations estimate energy barriers of  $\Delta E_1 = 1200$  K and  $\Delta E_2 = 2000$  K for reactions (1) and (2), respectively (see Graninger et al. 2014, for a full discussion). Recent chemical models demonstrate, however, that the observed  $X(\text{HCN})/X(\text{HNC})$  variations in the vicinity of the ONC can be explained if the  $\text{HNC} + \text{H}$  reaction (1) poses an energy barrier of  $\Delta E_1 = 200$  K, that is, approximately an order of magnitude

lower than previously estimated (Graninger et al. 2014). A similarly low energy barrier has been proposed for the  $\text{HNC} + \text{O}$  reaction (2) (Jin et al. 2015). Nevertheless, no observational nor theoretical work has quantified this latter energy barrier in detail to-date.

In Figure 4 (upper panel) we display the observed variations of the  $I(\text{HCN})/I(\text{HNC})$  intensity ratio in Orion, this time as function of  $1/T_K$  (grey crosses). We colour-code those positions with accurate temperature estimates (with  $\delta T_K \leq 5\%$ ) according to their  $\text{H41}\alpha$  intensity in Fig. 1 as indication of their proximity to the ONC. Two separate regimes can be clearly distinguished in this plot. At  $T_K \gtrsim 50$  K, those positions directly exposed to the HII nebula (i.e., showing large values of  $\text{H41}\alpha$  emission) show a rapid variation of  $I(\text{HCN})/I(\text{HNC})$  ratio as function of  $T_K$ . On the other hand, those cloud positions without significant  $\text{H41}\alpha$  emission present a much shallower dependence for temperatures  $T_K \sim [10, 50]$  K. Interestingly, this trend seems to continue down to the typical initial branching ratios ( $\sim [0.5, 1.0]$ ) found in dense cores (grey triangles; Hirota et al. 1998). These distinct slopes suggest the presence of two independent mechanisms controlling the observed  $I(\text{HCN})/I(\text{HNC})$  variations with a surprising low dispersion (see the narrow spread of our measurement for a given  $1/T_K$  value in our plot).

Compared to Fig. 3, the use of  $1/T_K$  units in Figure 4 allows to directly estimate the potential impact of different energy barriers for reactions (1) and (2). Assuming that  $\left(\frac{I(\text{HCN})}{I(\text{HNC})}\right) = \left(\frac{X(\text{HCN})}{X(\text{HNC})}\right)$  (see Appendix A for a full discussion), the value of  $\Delta E_i$  can be directly obtained from the linear fit of  $\left(\frac{X(\text{HCN})}{X(\text{HNC})}\right) = A \times \exp\left(\frac{-\Delta E_i}{T_K}\right)$ , that is,  $\log_{10}\left(\frac{I(\text{HCN})}{I(\text{HNC})}\right) \propto \frac{-\Delta E_i}{T_K}$  under this representation. As denoted in this figure (black dashed line), our observations reproduce the previously proposed steep dependence of the  $I(\text{HCN})/I(\text{HNC})$  ratio at high temperatures found within the ONC region using  $\Delta E_1 = 200$  K (black dashed line Schilke et al. 1992; Graninger et al. 2014). These results are expected as the  $\text{HNC} + \text{H}$  reaction (1) is favoured by the large amount of free H-atoms generated within the HII region.

On the other hand, the shallower dependence shown in Fig. 4 (upper panel) at low temperatures suggests a much lower energy barrier for the corresponding  $\text{HNC} + \text{O}$  reaction (2). A series of manual fits to our data indicate an energy barrier for this latter reaction on the order of  $\Delta E_2 \sim 10$  K (red line). If confirmed, the chemical destruction of HNC via  $\text{HNC} + \text{O}$  reaction could potentially dominate the observed  $I(\text{HCN})/I(\text{HNC})$  intensity variations at  $T_K < 50$  K within clouds.

We quantified the energy barriers in reactions (1) and (2) using a grid of standard chemical models. Our chemical models use the code and network from Bosman et al. (2018). The chemical network is based on gas-phase reactions from the RATE12 network from the UMIST Database for Astrochemistry<sup>6,7</sup> (Garrod et al. 2008; McElroy et al. 2013; Walsh et al. 2015). Binding energies were taken from (Penteado et al. 2017). The reaction rate coefficient for reaction (1) was replaced and reaction (2) was added to the network both with the values from Graninger et al. (2014).

For our study, we created a set of four model grids (Models 1-4) using different combinations of  $(\Delta E_1, \Delta E_2)$  values (see below) and track their evolution with time. Using the same chemical network, our goal is to isolate the effects of distinct energy

<sup>6</sup> Grain surface reactions from the Ohio State University (OSU) network: <http://faculty.virginia.edu/ericherb/research.html>

<sup>7</sup> <http://www.udfa.net>

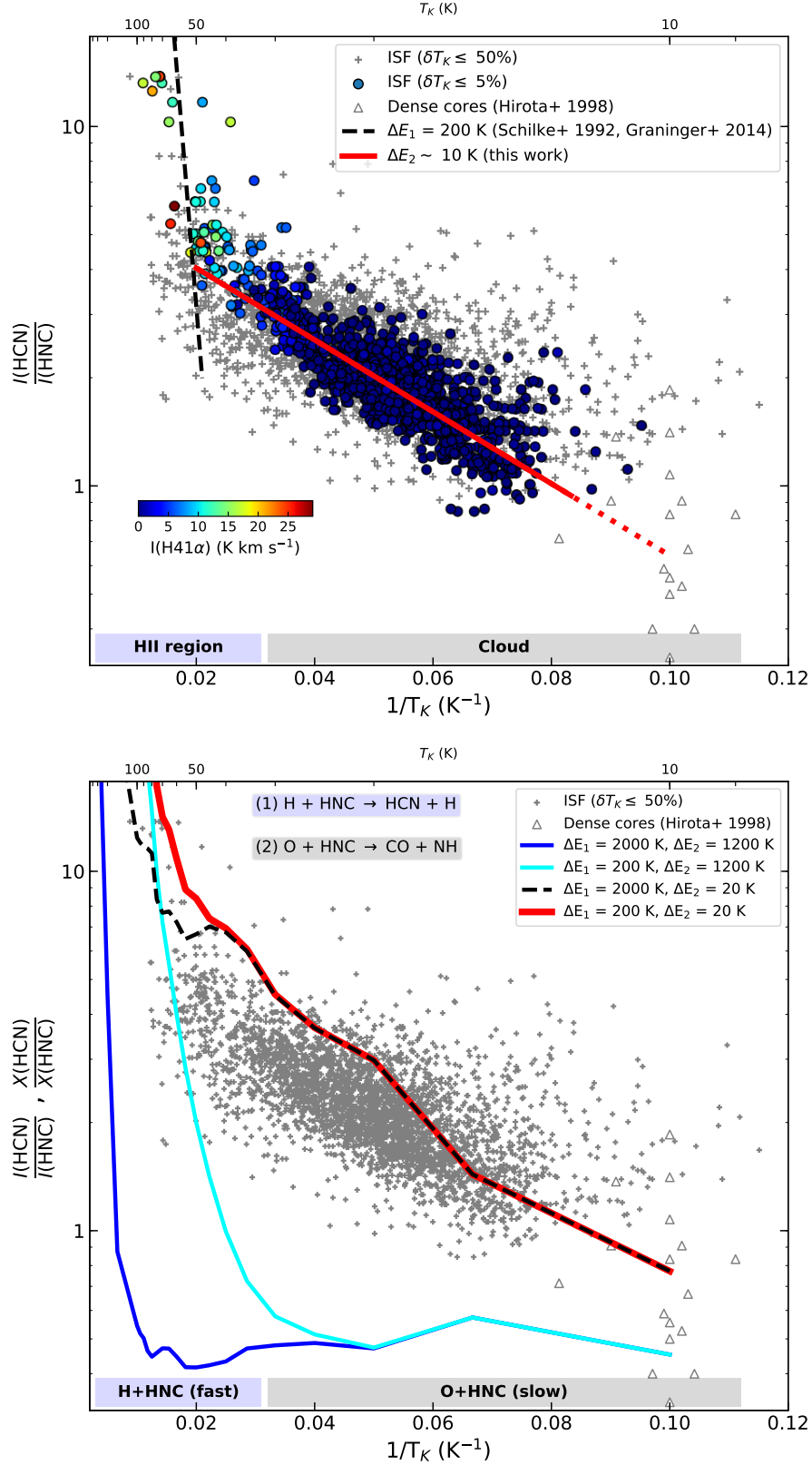


**Fig. 4. (Upper panel)** Observed dependence of the  $I(\text{HCN})/I(\text{HNC})$  intensity ratio as function of  $1/T_K$  in the ISF (grey crosses; this work) in comparison with classical estimates from dense core surveys (grey triangles; Hirota et al. 1998). The positions with good temperature estimates (i.e.,  $\delta T_K/T_K \leq 5\%$ ) are colour coded according to their total  $\text{H41}\alpha$  intensity (see Fig. 1). The temperature dependence of the  $I(\text{HCN})/I(\text{HNC})$  ratio expected for an energy barrier of  $\Delta E_1 = 200 \text{ K}$  for reaction 1 is indicated by a black dashed line (Schilke et al. 1992; Graninger et al. 2014). Similarly, the newly proposed low energy barrier for  $\Delta E_2 = 10 \text{ K}$  for reaction 2 is shown in red. **(Lower panel)**  $X(\text{HCN})/X(\text{HNC})$  abundance variations predicted by our Models (1-4) with different energy barriers (see also text) compared to the observed intensity variations in cores (grey triangles) and across the ISF (grey crosses). Our model results illustrate the different dominant roles of reactions (1) and (2) determining the temperature structure of the ONC (blue area) and the rest of the cloud (grey area), respectively. The detailed equivalence between the observed intensity ratios and the corresponding abundance ratios in our models are discussed in Appendix B.

barriers on the observed isometric fractionation as function of temperature. We evaluate the corresponding  $X(\text{HCN})/X(\text{HNC})$  abundance ratio in these models at temperatures between  $T_K = [10, 1000]$  K sampled with 20 points per dex in log-scale. In all cases, we assume a typical evolutionary timescale of  $\tau = 0.5$  Myr, a density of  $n(\text{H}_2) = 10^4 \text{ cm}^{-3}$ , and a standard cosmic ionization rate of  $\zeta = 10^{-17} \text{ s}^{-1}$ . These fiducial parameters are meant to capture the overall dependence of the HCN/HNC abundance variations under standard ISM conditions (see below). For completion, we describe the variations respect to these fiducial models as function of time, density, and cosmic-ray ionization in Appendix B.

We compared the  $X(\text{HCN})/X(\text{HNC})$  abundances ratios predicted by our chemical Models 1-4 with the observed  $I(\text{HCN})/I(\text{HNC})$  intensity variations in Orion (grey crosses) in Figure 4 (lower panel; colour lines). The properties of these models can be summarized as follow:

- Model 1 uses the classical energy barriers estimated by ab-initio calculations, namely,  $\Delta E_1 = 2000$  K and  $\Delta E_2 = 1200$  K (dark blue line). With both reactions (1) and (2) inhibited by their high energy barriers, Model 1 shows no abundance variation respect to the original HCN/HNC branching value at the temperatures surveyed in Orion (i.e.,  $T_K \ll \Delta E_i$ ) contrary to our observations.
- Model 2 assumes a  $\Delta E_1 = 200$  K while keeps  $\Delta E_2 = 1200$  K (cyan line). In close agreement to the results proposed by Graninger et al. (2014), the effects of the low energy barrier in the  $\text{H} + \text{HNC}$  reaction explain the rapid increase of  $X(\text{HCN})/X(\text{HNC})$  observed at high temperatures. In this Model 2, however, this reaction (1) alone fails to reproduce the observed temperature dependence at cloud temperatures of  $T_K \lesssim 50$  K.
- Model 3 quantifies the impact of a low energy barrier for the  $\text{O} + \text{HNC}$  reaction (2) assuming a  $\Delta E_2 = 20$  K in the absence of reaction (1) suppressed by a  $\Delta E_1 = 2000$  K (dashed black line). These calculations demonstrate the dominant role of reaction (2) at low temperatures. As predicted by our linear fits (see above), Model 3 reproduces the smooth increase of the  $X(\text{HCN})/X(\text{HNC})$  ratio with temperature within  $10 \text{ K} \lesssim T_K < 50 \text{ K}$ . On the contrary, this model underestimates the much stronger temperature dependence observed at  $T_K > 50$  K in HII regions like the ONC.
- Finally, Model 4 explores the combined effects of low energy barriers in both reactions (1; Model 2) plus (2; Model 3) adopting barriers with  $\Delta E_1 = 200$  K and  $\Delta E_2 = 20$  K, respectively (solid red line). In remarkably close agreement with our observations, Model 4 simultaneously reproduces both low- and high-temperature variations on the  $I(\text{HCN})/I(\text{HNC})$  ratios in Orion. Moreover, it connects these results with the reported abundance ratios in dense cores.

Our chemical models demonstrate the relative importance of the different HNC destruction mechanisms with low energy barriers determining the observed  $I(\text{HCN})/I(\text{HNC})$  variations in clouds like Orion. In agreement to previous results (Schilke et al. 1992; Graninger et al. 2014), warm and irradiated (HII) regions such as the ONC are largely dominated by the isomerization of HNC into HCN via  $\text{H} + \text{HNC} \rightarrow \text{HCN} + \text{H}$ . Outside these active regions, our models suggest that the additional destruction of HNC via  $\text{O} + \text{HNC} \rightarrow \text{NH} + \text{CO}$  reaction is the most likely driver of the reported  $I(\text{HCN})/I(\text{HNC})$  variations at lukewarm temperatures.

Both observational and model results consistently demonstrate that reactions (1) and (2) have much lower activation ener-



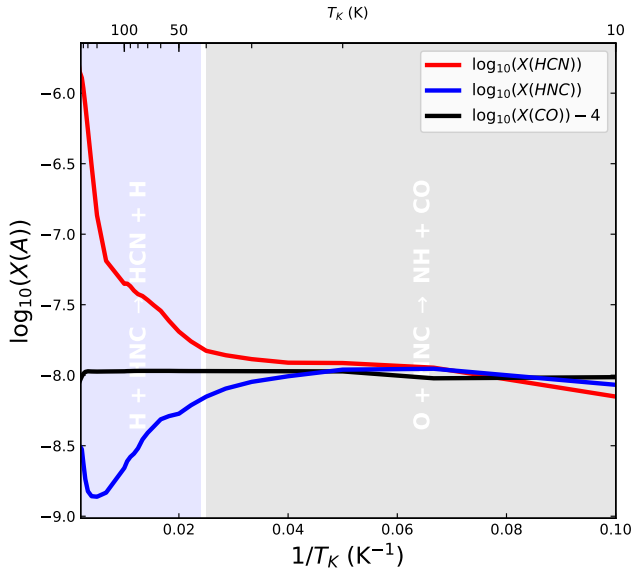


**Fig. 5.** Temperature variations of the absolute abundance for HCN (red), HNC (blue), and  $^{12}\text{CO}$  (black) predicted by our Model 4. The range of influence of the  $\text{HNC} + \text{H}$  (reaction 1) and  $\text{HNC} + \text{O}$  (reaction 2) destruction mechanisms are indicated in blue and gray coloured areas, respectively.

gies than previously estimated. Our Orion data confirm the previously proposed  $\Delta E_1 = 200$  K barrier for the  $\text{H} + \text{HNC}$  reaction (Graninger et al. 2014). In addition, the large dynamic range of our data at intermediate temperatures indicates the presence of an almost barrier-less activation energy for the  $\text{O} + \text{HNC}$  reaction. Determining its precise value is, however, made difficult by the apparent scatter ( $\sim 0.2$  dex) in our data and the potential observational biases on the comparison between intensity and abundance ratios (see an extensive discussion about these comparisons in Appendix A). Nonetheless, the unprecedented dynamic range of our data suggests an observational constraint on the energy barrier for reaction (2) of approximately  $\Delta E_2 \sim 20$  K. Additional characterization of multiple HCN and HNC isotopologues, together with dedicated chemical models, are therefore needed to accurately quantify this barrier (e.g., see Schilke et al. 1992).

### 3.4. HCN/HNC abundance variations: evolution and steady-state

Our chemical models allow us explore in high detail the origin of the observed temperature dependence of the  $X(\text{HCN})/X(\text{HNC})$  ratio found in Sect. 3.3. Figure 5 shows the individual gas phase abundances of HCN (red) and HNC (blue) respect to  $\text{H}_2$  (i.e.,  $X(\text{A})=X(\text{A})/X(\text{H}_2)$ ) as function of temperature obtained in our previous Model 4 (see Fig. 4, lower panel). At  $T_K = 10$  K (or  $1/T_K = 0.1 \text{ K}^{-1}$ ), both isomers show similar absolute abundances of  $X(\text{HCN}) \sim X(\text{HNC}) = 10^{-8}$  as expected from the initial branching. The abundance variations of these two species are compared to the relative amount of CO (black), a reference molecule with almost constant abundance of  $X(\text{CO}) \sim 10^{-4}$  at all temperatures in our models. The changes on the HCN and HNC abundances clearly illustrate the relative influence of reactions (1) and (2) explaining the two separated temperature regimes observed in Fig. 4. At low  $T_K$  (or high  $1/T_K$ ), the smooth increase

on the observed  $X(\text{HCN})/X(\text{HNC})$  ratio is dominated by the reduction of the HNC abundance, up to 0.25 dex, after the recombination of this molecule with O in reaction (2). This selective destruction of HNC is exacerbated after the activation of reaction (1) and the subsequent production of HCN at higher temperatures. Together, the resulting  $X(\text{HCN})/X(\text{HNC})$  abundance ratio rapidly increases by more than one order of magnitude at  $T_K > 40$  K (or  $1/T_K < 0.025 \text{ K}^{-1}$ ).

During their early evolution of our models the destruction of HNC also proceeds at different speeds within each of the two temperature regimes identified before. Due to the large reservoir of free H atoms, the isomerization of HNC via reaction (1) occurs on short timescales of  $\tau \sim 0.1$  Myr, rapidly dominating the destruction of this molecule at high temperatures. On the other hand, the recombination of O + HNC depends largely on the more limited atomic O reservoir regulated by the combined effect of gas density and cosmic-ray ionization (see Appendix B). Under the normal ISM conditions described in our Model 4, reaction (2) proceeds at slower rates becoming relevant only at  $\tau > 0.3$  Myr.

Despite their different initial speeds, both HNC destruction reactions reach a steady-state at later times in our models. For a given set of energy barriers, and independently of their density and cosmic-ray ionization, the observed  $X(\text{HCN})/X(\text{HNC})$  ratio in our simulations follows an almost identical temperature dependence at timescales  $\tau \geq 0.5$  Myr. This functional dependence remains unaltered in our models until the end of our simulations at  $\tau = 3$  Myr (see Appendix B for a discussion). These results suggest a (pseudo-)equilibrium between the formation and destruction mechanisms of both HCN and HNC isomers. This stable configuration could explain the low dispersion observed in the  $\geq 1$  Myr-old gas in Orion.

## 4. A new chemical thermometer for the ISM

In Sect. 3.2 and 3.3 we investigated the origin of the large variations of the observed  $I(\text{HCN})/I(\text{HNC})$  intensity ratio for their  $J=1-0$  lines in Orion. As illustrated by our models, these intensity differences correspond to actual changes on the relative abundances of both HCN and HNC isomers due to the selective destruction of HNC. These abundance variations are independent of the gas density and, after short timescales ( $\sim 0.3$  Myr), become invariant with time. The systematic dependence shown in our data indicates that the absolute value of the reported  $I(\text{HCN})/I(\text{HNC})$  intensity ratios is primarily determined by the temperature dependence of reactions 1 and 2. In this section, we discuss how these observational variations can be employed as direct measurement of the gas kinetic temperatures of the molecular gas in the ISM.

### 4.1. Calibration: empirical correlation between HCN/HNC and $T_K$

As shown by the first-order linear fits in Fig. 3 (solid and dashed red lines), the correlation between the total (aka including all hyperfine components) observed  $I(\text{HCN})/I(\text{HNC})$  intensity ratios and gas kinetic temperatures  $T_K$  can be described by a two-part linear function following:

$$T_K[\text{K}] = 10 \times \left[ \frac{I(\text{HCN})}{I(\text{HNC})} \right] \quad \text{if} \quad \left( \frac{I(\text{HCN})}{I(\text{HNC})} \right) \leq 4 \quad (3)$$

and

$$T_K[\text{K}] = 3 \times \left[ \frac{I(\text{HCN})}{I(\text{HNC})} - 4 \right] + 40 \quad \text{if} \quad \left( \frac{I(\text{HCN})}{I(\text{HNC})} \right) > 4 \quad (4)$$

At low intensity ratios  $1 < I(\text{HCN})/I(\text{HNC}) \leq 4$ , the goodness of our fit demonstrates that Eq. 3 accurately predicts the thermal gas conditions of the gas at lukewarm temperatures with errors of  $\Delta T_K \lesssim 5$  K. These uncertainties seem to grow at  $I(\text{HCN})/I(\text{HNC}) \lesssim 1$  describing low-temperature regimes of  $T_K \lesssim 10$  K, likely due to the combination of excitation and opacity effects. On the other hand, Eq. 4 is suggested for  $I(\text{HCN})/I(\text{HNC}) > 4$  in order to obtain rough estimates of higher gas temperatures, despite its relatively larger uncertainties with  $\Delta T_K > 10$  K. Part of this latter discrepancies could be generated by the limited sensitivity of the low rotational transitions of  $\text{NH}_3$  when tracing gas temperatures above  $T_K > 50$  K (Tang et al. 2017).

The empirical calibration of Equations 3 and 4 introduces a simple method to estimate the gas kinetic temperatures. Thanks to their large abundances and favourable excitation conditions, HCN and HNC are two of the most observed molecular tracers in current line surveys, easily detectable in local and extragalactic studies alike (e.g., Pety et al. 2017). Due to their proximity in frequency, transitions such as HCN (1-0) and HNC (1-0) can also be simultaneously observed using standard broad band receivers (e.g., Fig. 1). Our results demonstrate the direct use of the  $I(\text{HCN})/I(\text{HNC})$  line ratio as proxy of the gas kinetic temperature within clouds across a wide range of physical conditions (see also Sects. 4.2 and 4.4). Readily obtained at large-scales, the proven sensitivity of this straightforward observable opens a novel window on the study of the thermal gas properties of the ISM without the need of any chemical nor radiative transfer model. Moreover, and unlike the dust emission, this method offers the possibility of studying the temperature structure of the different gas components superposed along the line-of-sight when resolved in velocity. In summary, we propose the use of the empirical correlations described by Eqs. 3 and 4 as a new chemical thermometer of the molecular gas in ISM with an optimal working range between  $15 \text{ K} \lesssim T_K \leq 40 \text{ K}$ .

#### 4.2. Application: gas temperature map of the Orion ISF

We have tested the use of the proposed  $I(\text{HCN})/I(\text{HNC})$  line ratio as temperature probe from the analysis of our own data in Orion. For each position in our maps with detected emission in each of the HCN and HNC isomers  $I(\text{HCN}), I(\text{HNC}) \geq 1.0 \text{ K km s}^{-1}$  we calculate the gas kinetic temperature  $T_K(\text{HCN}/\text{HNC})$  according to Equations 3 and 4. We present the resulting temperature maps in Figure 2d. An inspection of Fig. 2 reveals the potential of this new technique for the study of the thermal structure of clouds such as Orion. As illustrated by this figure, the observed  $I(\text{HCN})/I(\text{HNC})$  variations capture the well known large temperature differences between the warm ONC region and the much colder surrounding cloud material. In particular, our maps show the systematic temperature differences along the ISF when comparing the warm OMC-1/2/3 regions with the colder OMC-4/4S clouds. Although calculated on a point-to-point basis, the observed HCN/HNC derived temperatures present a smooth spatial variation denoting the good behaviour of these measurements across our maps.

We have quantified the performance of our HCN/HNC temperature estimates (Fig. 2d) in comparison to the previously derived temperatures maps obtained from ammonia observations (Friesen et al. 2017) (Fig. 2c). Overall, our HCN/HNC estimates partially resolve the rapid increase of the gas kinetic temperature in the OMC-1 region towards the Trapezium stars and the ONC, showing consistent gas temperatures  $T_K > 30 \text{ K}$ . Nonetheless, our measurements underestimate the extreme temperatures

found around the Orion BN/KL region as well as in the Orion Bar detected in warm  $\text{NH}_3$ . This is not surprising given the larger uncertainties of our method at the high temperature regimes described by Eq.4 above  $T_K > 40 \text{ K}$  (see Sect.4). Outside these problematic areas, our HCN/HNC temperature measurements show a remarkably close agreement with previous  $\text{NH}_3$  estimates. In particular, we find an excellent correlation between the absolute and relative variations of these two temperatures estimates in those dense and cold regions such as cores and filaments with significant  $\text{N}_2\text{H}^+$  emission (enclosed by a black contour in our maps in Fig. 2; see Hacar et al. 2017a, 2018).

In addition, the detection of both HCN and HNC isomers at large scales allows to investigate the temperature structure of the gas at low column densities. As shown in Fig. 2d, our  $T_K(\text{HCN}/\text{HNC})$  measurements extend far beyond those regions with  $\text{N}_2\text{H}^+$  or  $\text{NH}_3$  detections. In particular, the significant increase of temperature measurements towards low density regions such as OMC-4/4S is noteworthy. Interestingly, our estimates show a rapid increase in the gas temperature to values above  $T_K \gtrsim 30 \text{ K}$  in those regions with no detected dense gas.

#### 4.3. Validation: comparison with other temperature estimates in Orion A

The temperature structure of both gas and dust in Orion A cloud have been widely investigated in the past using large-scale molecular line and continuum observations (Nakamura et al. 2012; Shirley 2015; Nishimura et al. 2015; Friesen et al. 2017). Figure 6 shows our  $T_K(\text{HCN}/\text{HNC})$  measurements (Fig. 6) together with other classical temperature estimates based on observations of  $\text{NH}_3$  (Fig. 6b),  $^{12}\text{CO}$  (Fig. 6c), and Herschel (Fig. 6d) within the same area as our IRAM data. In Sections 4.3.1-4.3.3 we quantify the performance and dynamic range of our empirical  $T_K(\text{HCN}/\text{HNC})$  measurements as proxy of the gas kinetic temperatures in the ISM in comparison to these previous results.

##### 4.3.1. HCN/HNC vs. $\text{NH}_3$

Together with their corresponding maps (Figs. 6a-b), in Figure 7 (central panel) we illustrate the temperature variations in the predicted  $T_K(\text{HCN}/\text{HNC})$  values in our IRAM30m observations with respect to the measured total gas column densities (in units of  $A_V$ ) derived by Lombardi et al. (2014) in Orion using *Herschel* observations (red triangles)<sup>8</sup>. For simplicity we display only those positions outside the Orion HII nebula identified by presenting  $I(\text{H41}\alpha) \leq 1.0 \text{ K km s}^{-1}$ . We observe a systematic decrease of the recovered  $T_K(\text{HCN}/\text{HNC})$  gas temperatures at increasing column densities, from about  $T_K \sim 35 \text{ K}$  at  $A_V \sim 5$  mag to  $T_K \sim 12 \text{ K}$  at  $A_V \sim 50$  mag, as expected for an externally irradiated cloud. At higher column densities, our estimates appear to be also sensitive to the internal gas heating produced by the embedded protostars within clouds such as OMC-2/3 (see warm spots in our maps along these regions).

Both maps (Fig. 6b) and statistics (Fig. 7) highlight the enhanced dynamic range of our  $T_K(\text{HCN}/\text{HNC})$  temperature estimates. From the total 8650 Nyquist spectra in our observations, 8092 of these positions (93%) present  $I(\text{HCN}), I(\text{HNC}) \geq 1.0 \text{ K km s}^{-1}$  being suitable for our temperature calculations. These numbers contrast with the much more limited  $\text{NH}_3$  measurements, only present in 3469 positions

<sup>8</sup> The originally derived  $A_K$  values provided by Lombardi et al. (2014) are converted into  $A_V$  units following the same procedure described in Hacar et al. (2017b).

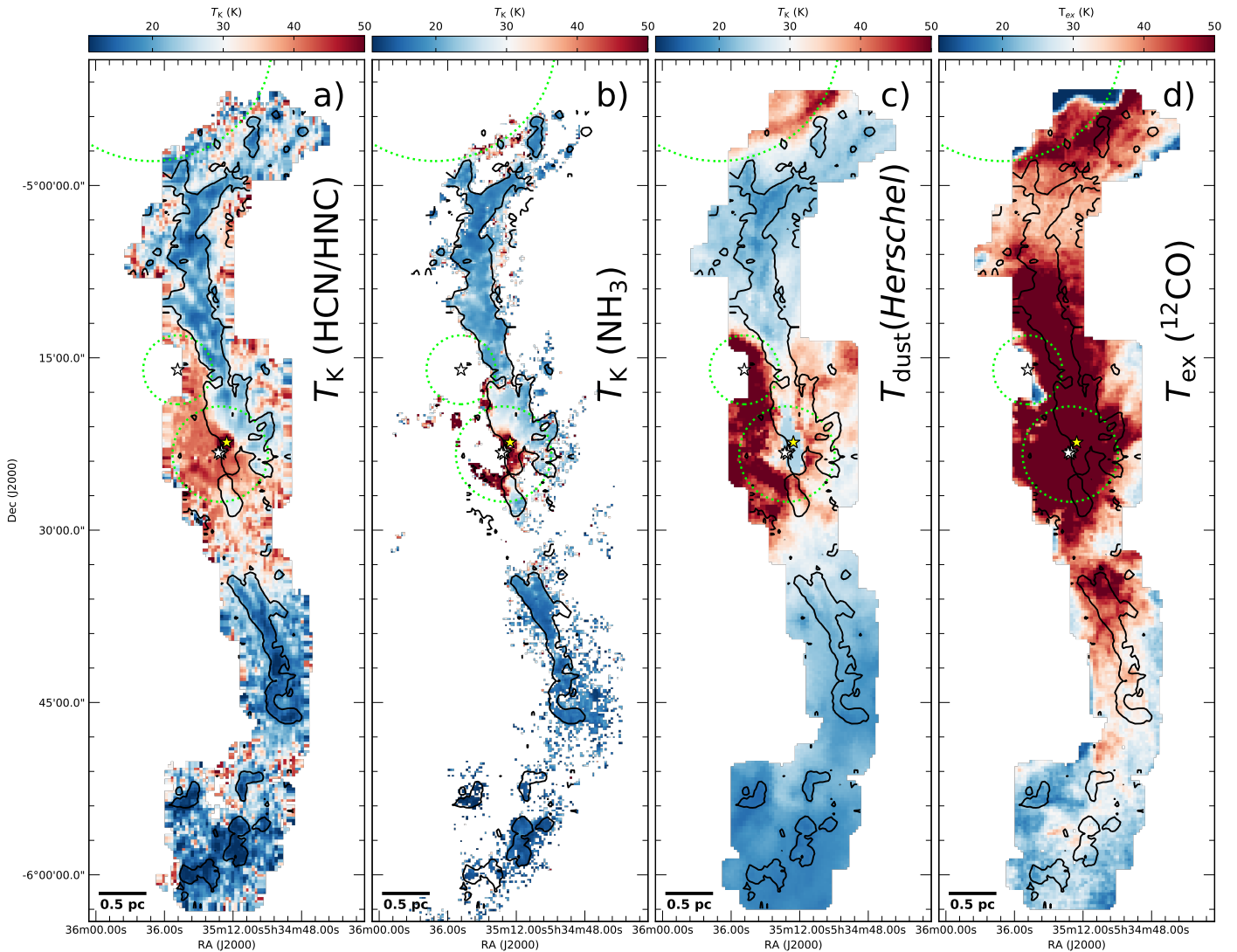


**Fig. 6.** Comparison between different  $T_K$  estimates along the ISF: (a)  $T_K(\text{HCN}/\text{HNC})$  (this work), (b) ammonia-derived gas kinetic temperatures  $T_K(\text{NH}_3)$  (Friesen et al. 2017), (c) Herschel dust temperatures  $T_{\text{dust}}$  (Lombardi et al. 2014), and (d)  $^{12}\text{CO}$  (1–0) excitation temperatures  $T_{\text{ex}}(^{12}\text{CO})$  (Nakamura et al. 2012; Shimajiri et al. 2014), all represented with the same colour scale. We note that both dust temperature and column density are underestimated towards the OMC-1 and BN/KL regions due to saturation effects and the lack of proper spectral energy distribution (SED) fits in the Herschel maps provided by Lombardi et al. (2014). Also we notice the rapid decrease of the  $T_{\text{ex}}(^{12}\text{CO})$  at the northern end our maps, likely due to subthermal excitation of the  $^{12}\text{CO}$  (i.e.,  $T_{\text{ex}}(^{12}\text{CO}) < T_K$ ) lines at the low densities expected in this region. To facilitate the comparison of these figure, we indicate the intensity contour with  $I(\text{N}_2\text{H}^+) = 1.5 \text{ K km s}^{-1}$  in panels (b-d). Circles and star symbols are similar to Fig. 1.

within the same region, or 40% of the total map coverage. In the histograms shown in Fig. 7 we display a direct comparison of the temperature (right panel) and column density (upper panel) regimes recovered by these  $T_K(\text{HCN}/\text{HNC})$  (red) and  $T_K(\text{NH}_3)$  (blue) measurements. Similar to  $\text{NH}_3$ , our  $\text{HCN}/\text{HNC}$  observations homogeneously trace the low gas temperatures ( $T_K \lesssim 20 \text{ K}$ ) of high column density ( $A_V > 20 \text{ mag}$ ) material. In a clear improvement compared to  $\text{NH}_3$ , however, our  $T_K(\text{HCN}/\text{HNC})$  temperature measurements show a significantly larger sensitivity towards warmer regions ( $T_K > 30 \text{ K}$ ) at low column densities  $A_V < 10 \text{ mag}$ .

#### 4.3.2. HCN/HNC vs. dust

The use of dust effective temperatures  $T_{\text{dust}}$  obtained by different *Herschel* observations (Lombardi et al. 2014) allows the study of the gas kinetic temperatures at different density regimes in clouds not detected in  $\text{NH}_3$ . This comparison can potentially

be altered by the density dependence of the gas-to-dust thermal coupling (e.g., Goldsmith 2001) as well the distinct line-of-sight effects weighted by these two measurements. Despite these caveats, the relative variations of these two observables could be used to quantify the performance of this technique across a wide range of temperatures and densities, at least in a first order approximation.

We compared both gas and dust temperature measurements from Figures 6a and 6c, respectively. Overall, both  $T_K(\text{HCN}/\text{HNC})$  and  $T_{\text{dust}}$  estimates show roughly similar variations across our maps. Significant differences between these estimates (and  $\text{NH}_3$ ) are seen under extreme conditions, both at low temperatures  $T_K < 15 \text{ K}$  in some of the densest regions within this cloud (denoted by their  $\text{N}_2\text{H}^+$  emission) as well as above  $T_K > 50 \text{ K}$  in the warmest nebulae in this cloud (e.g., ONC). Nonetheless, we observe a good correspondence between our  $T_K(\text{HCN}/\text{HNC})$  estimates and the derived  $T_{\text{dust}}$  values across the ISF, particularly at intermediate and low column densities.

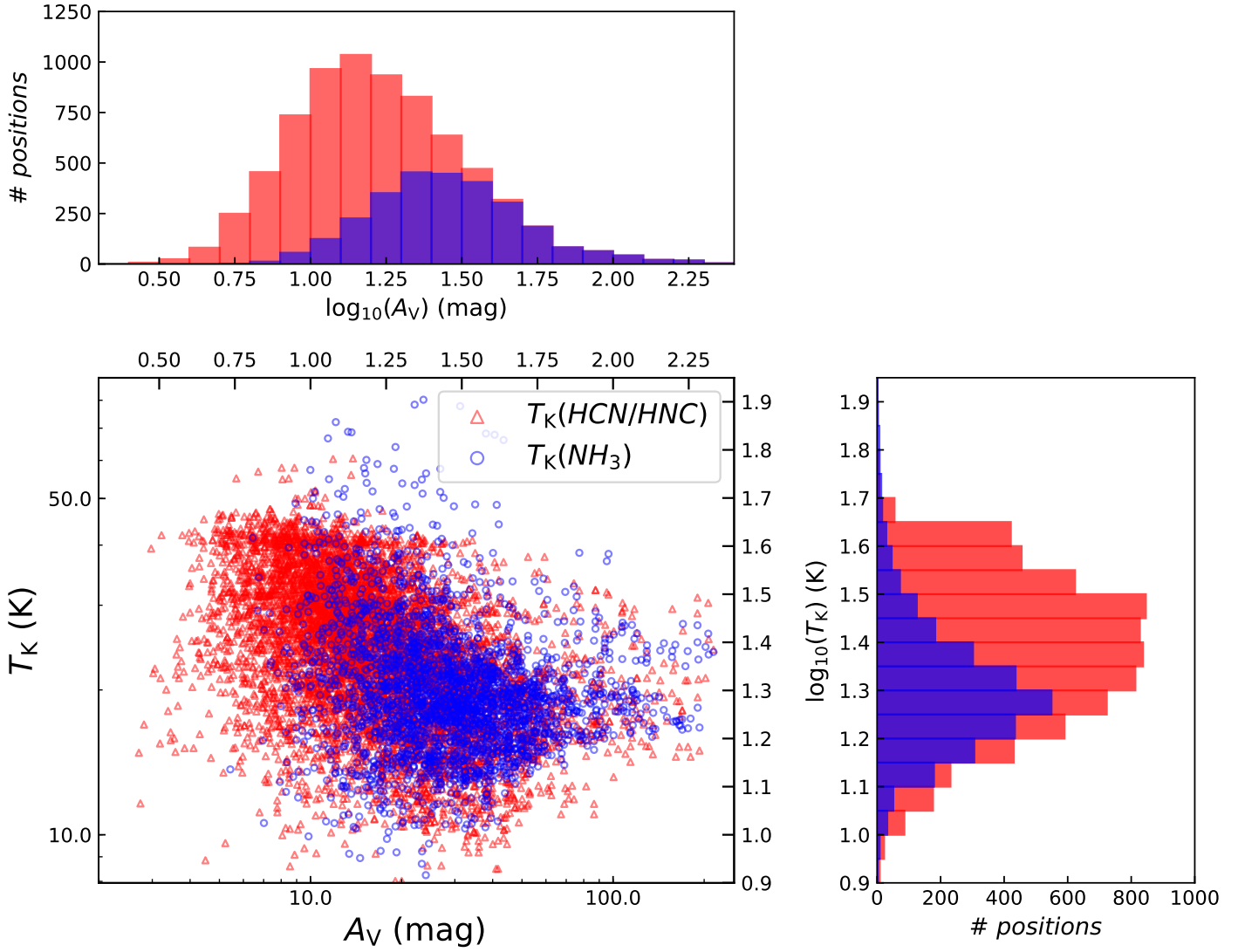


**Fig. 7. (Central panel)** Gas kinetic temperatures derived using both  $T_K(\text{HCN}/\text{HNC})$  (red triangles) and  $T_K(\text{NH}_3)$  estimates as function of total gas column density (Lombardi et al. 2014) in the ISF region. For simplicity, we display only those positions outside the Orion HII nebula (i.e.,  $I(\text{H}41\alpha) \leq 1.0 \text{ K km s}^{-1}$ ). **(Lateral panels)** Histograms for the distribution of both temperatures (right subpanel) and column densities (upper subpanel) traced by each of these  $T_K(\text{HCN}/\text{HNC})$  (red bars) and  $T_K(\text{NH}_3)$  (blue bars) measurements. Note that the histograms are binned in log-space.

In Figure 8a, we display a point-by-point comparison between the gas and dust temperature estimates at all positions with  $I(\text{HCN}), I(\text{HNC}) \geq 1.0 \text{ K km s}^{-1}$  in the ISF outside of the ONC nebula. We find a good correlation between the  $T_K(\text{HCN}/\text{HNC})$  and  $T_{\text{dust}}$  variations in the ISF both in relative and absolute terms, almost following a 1:1 relationship (dashed line) with no significant dependence on the corresponding total gas column density. More than 50% of our  $T_K(\text{HCN}/\text{HNC})$  estimates present similar values to their corresponding  $T_{\text{dust}}$  measurements with deviations of less than  $\pm 5 \text{ K}$  (see dotted lines). This agreement is particularly striking within the optimal temperature range of our method.

Taken together, theoretical (Sect. 4) and empirical (Fig. 7) arguments demonstrate the robustness of the observed total  $I(\text{HCN})/I(\text{HNC})$  integrated intensity ratio as direct measurement of the  $T_K$  gas kinetic temperatures in a wide range of temperature and column density regimes. Only limited by the extension of our maps, this simple technique benefits from the bright emission of both HCN and HNC isomers in both dense and diffuse media (Pety et al. 2017; Kauffmann et al. 2017). Easily ob-

tained in regular millimeter line observations, this simple observable opens a new window on the study of the gas thermal properties of clouds at parsec scales.

#### 4.3.3. HCN/HNC vs. CO

As for the dust, observations of diffuse tracers such as  $^{12}\text{CO}$  provide information of the thermal structure of clouds at large scales. For any emission line, its observed peak temperature ( $T_{\text{peak}}$ ) is connected to its excitation temperature ( $T_{\text{ex}}$ ) as well as its line opacity ( $\tau$ ), according to the radiative transfer equation  $T_{\text{peak}} = (J(T_{\text{ex}}) - J(T_{\text{bg}}))(1 - e^{-\tau})$ , where  $J(T) = \frac{h\nu/k}{\exp(h\nu/kT) - 1}$  and  $T_{\text{bg}}$  corresponds to the background temperature. In the optically thick regime ( $\tau \gg 1$ ), this equation can be simplified to obtain a direct measurement of the gas excitation temperature as:

$$T_{\text{ex}} = \frac{h\nu/k}{\ln\left(\frac{h\nu}{k(T_{\text{peak}} + J(T_{\text{bg}}))}\right) + 1} \quad (5)$$



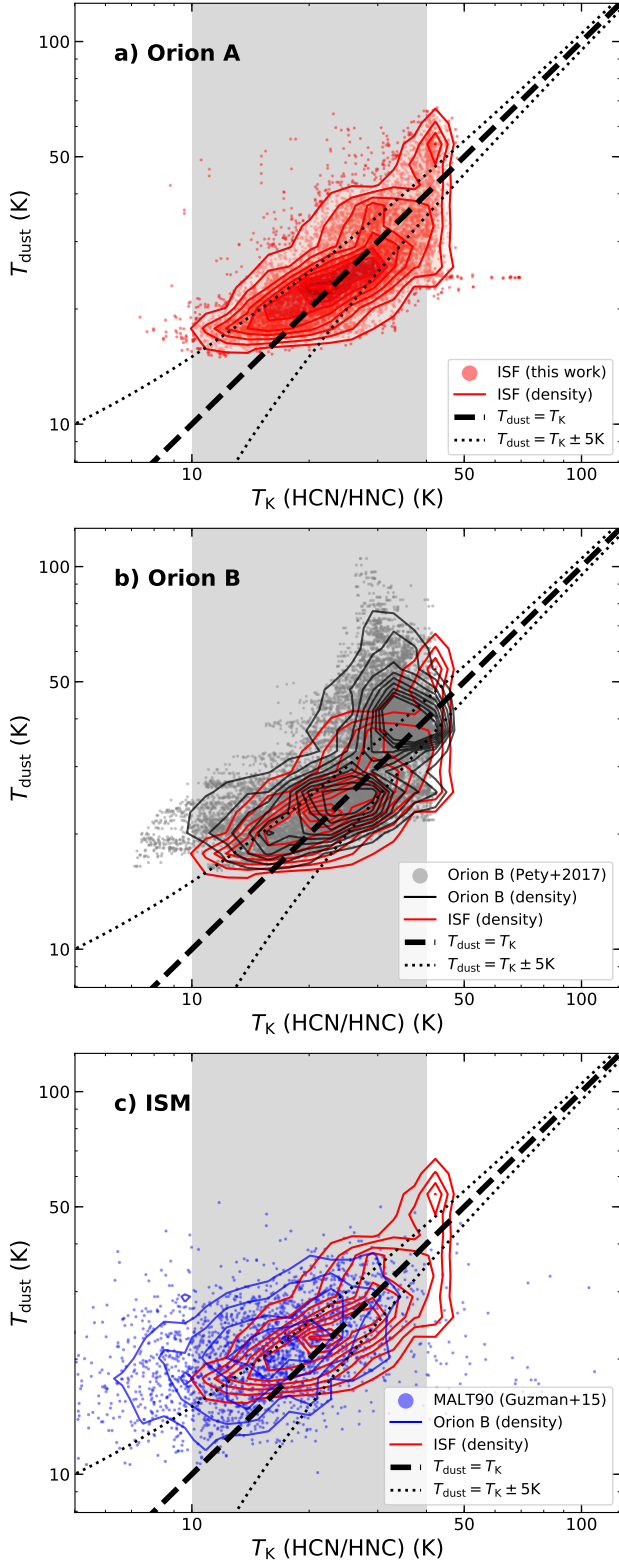


**Fig. 8.** Comparison between the  $T_K(\text{HCN}/\text{HNC})$  gas kinetic temperatures predicted by our empirical method and the observed dust temperatures in different environments and surveys: (a) Orion ISF (this work), (b) Orion B (Pety et al. 2017), and (c) MALT90 sample (Jackson et al. 2013; Guzmán et al. 2015). We indicate the direct  $T_K = T_{\text{dust}}$  (dashed line) and  $T_K = T_{\text{dust}} \pm 5$  (dotted lines) correlations in all panels. The optimal temperature range for the application of our method, between  $\sim [10, 40]$  K, is highlighted in grey in all panels.

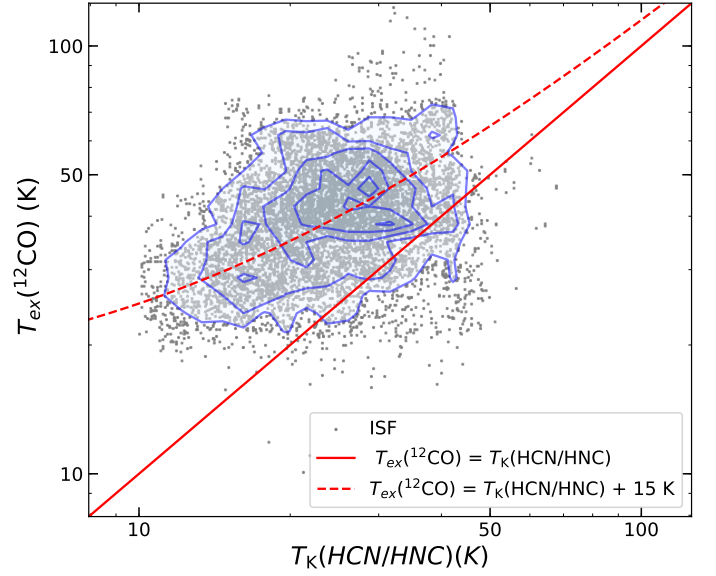


**Fig. 9.** Comparison between our new  $T_K(\text{HCN}/\text{HNC})$  temperature estimates and the  $^{12}\text{CO}$  (1–0) excitation temperatures  $T_{\text{ex}}(^{12}\text{CO})$  (Nakamura et al. 2012; Shimajiri et al. 2014) in all positions along the ISF outside the ONC nebula Orion HII nebula (i.e.,  $I(\text{H41}\alpha) \leq 1.0 \text{ K km s}^{-1}$ ; grey dots). A solid line indicates a linear correlation between these two temperatures estimates  $T_{\text{ex}}(^{12}\text{CO}) = T_K(\text{HCN}/\text{HNC})$ . Although positively correlated (see density contours in blue), we notice that the  $T_{\text{ex}}(^{12}\text{CO})$  temperature estimates are systematically higher than the corresponding  $T_K(\text{HCN}/\text{HNC})$  values at the same position. For illustrative purposes we display the  $T_{\text{ex}}(^{12}\text{CO}) \sim T_K(\text{HCN}/\text{HNC}) + 15 \text{ K}$  line denoted by a dashed red line in our plot.

Favoured by its typically large opacities in dark clouds ( $\tau(^{12}\text{CO}) > 10$ ), the  $^{12}\text{CO}$  ( $J=1-0$ ) transition ( $\nu = 115.271 \text{ GHz}$ ) is one of the most commonly used tracers of the gas temperatures in the ISM under the assumption of LTE conditions for which  $T_K = T_{\text{ex}}(^{12}\text{CO}) = f(T_{\text{mb}}(^{12}\text{CO}))$ .

A large number of studies explored the excitation conditions of  $^{12}\text{CO}$  using large-scale observations in Orion (e.g., Nakamura et al. 2012; Shimajiri et al. 2014; Nishimura et al. 2015, among others). Figure 2 d shows the excitation temperature  $T_{\text{ex}}(^{12}\text{CO})$  of the  $^{12}\text{CO}$  ( $J=1-0$ ) line according to Eq.5 using the line peak temperatures provided by Shimajiri et al. (2014) within the same area explored by our IRAM30m observations. As necessary (although perhaps not sufficient) condition, the high gas densities expected along the ISF favours the thermalization of the observed  $^{12}\text{CO}$  lines in most of the observed positions within our maps. A quick comparison with previous Figs.2 a-c reveals large differences between these CO temperature estimates and the equivalent HCN,  $\text{NH}_3$ , and dust measurements, both in terms of distribution and absolute values. Overall,  $T_{\text{ex}}(^{12}\text{CO})$  presents warmer temperatures along the entire ISF. In particular, the observed  $T_{\text{ex}}(^{12}\text{CO})$  temperatures are dominated by the strong heating effects around the ONC, M43, and NGC1977 nebulae (see dotted green lines; see Nishimura et al. 2015). Also in regions such as OMC-1 or OMC-2 these  $T_{\text{ex}}(^{12}\text{CO})$  estimates show a small dynamic range in temperature less sensitive to the cloud structure showing almost no variation compared to the distribution of denser and colder material traced by other gas or dust measurements.

Figure 9 quantifies the differences between the derived  $T_K(\text{HCN}/\text{HNC})$  and  $T_{\text{ex}}(^{12}\text{CO})$  temperatures in all positions sampled in our ISF observations outside the ONC (see Fig. 6). As illustrated by this plot,  $T_{\text{ex}}(^{12}\text{CO})$  presents systematically

higher values than  $T_K(\text{HCN}/\text{HNC})$ , typically on the order of 15 K warmer (see dashed line in the plot). Despite a large scatter,  $T_K(\text{HCN}/\text{HNC})$  and  $T_{\text{ex}}(^{12}\text{CO})$  temperatures show a positive correlation within  $T_K(\text{HCN}/\text{HNC}) \sim 10\text{--}50$  K regime. Although different in absolute terms, this parallel evolution suggests a physical link between these temperature estimates within our maps.

The observed differences between these  $T_K(\text{HCN}/\text{HNC})$  and  $T_{\text{ex}}(^{12}\text{CO})$  temperature estimates (Fig. 9) can be explained by the different cloud depths traced in each of these measurements. By construction, the reported  $T_{\text{ex}}(^{12}\text{CO})$  values estimate the gas temperatures at the cloud depth in which the  $^{12}\text{CO}$  line becomes optically thick (i.e.,  $\tau(^{12}\text{CO}) > 1$ ). Due to the large  $^{12}\text{CO}$  abundance, the  $^{12}\text{CO}$  (1–0) line quickly saturates at low column densities in the outermost warmer layers of dense regions like Orion. On the other hand, optically thinner transitions such as HCN (1–0) and HNC (1–0) provide information from deeper and, thus, colder layers of gas within these regions (e.g., see anti-correlation between  $T_K$  and  $A_V$  in Fig. 7, central panel). Sensitive to distinct parcels of gas the simultaneous study of both  $T_K(\text{HCN}/\text{HNC})$  and  $T_{\text{ex}}(^{12}\text{CO})$  could be used to investigate different temperature layers and regimes within clouds.

#### 4.4. Universality: HCN/HNC as probe of the gas kinetic temperatures in the ISM

After Orion, it is fundamental to explore whether this newly proposed thermometer can be extrapolated for the analysis of other star-forming regions. Similar to the ISF (Sect. 4.2), we investigated the correlation between the  $T_K(\text{HCN}/\text{HNC})$  and  $T_{\text{dust}}$  temperatures in the Orion B cloud in Figure 8b. To produce this plot, we resampled and combined the HCN/HNC intensities provided by Pety et al. (2017) with the corresponding dust effective temperatures derived in Lombardi et al. (2014) (grey dots). These molecular data expand over a total area of  $\sim 1$  deg<sup>2</sup> within the central region of Orion B cloud, covering a wide range of star-forming and thermal conditions (see Pety et al. 2017). We converted each HCN/HNC intensity ratio into its corresponding gas kinetic temperature following our empirical prescriptions. Altogether, we find a good correspondence between the  $T_K(\text{HCN}/\text{HNC})$  values in Orion B predicted by our method and the expected  $T_{\text{dust}}$  variations (black contours). Deviations from this correlation are observed at temperatures  $> 30$  K, likely due to the limitations of our method in combination of line-of-sight effects. Nonetheless, we find a direct correspondence between the temperature estimates in Orion B and our Orion A results (red contours), both in dynamic range and absolute variations.

Testing the robustness this novel technique in other clouds is hindered by the limited access of simultaneous HCN, HNC, and  $T_{\text{dust}}$  maps. In the absence of large-scale observations similar to our Orion data, we have compared the predicted gas kinetic temperatures obtained using HCN/HNC line ratios with additional dust temperature estimates extracted from different molecular surveys across the Milky Way. In particular, we combined the observed  $I(\text{HCN})/I(\text{HNC})$  intensity ratios in dense clumps provided by the MALT90 (Jackson et al. 2013) and  $T_{\text{dust}}$  measurements described by Guzmán et al. (2015) (3216 sources). Several caveats should be considered for this comparison. Each MALT90 target corresponds to a parsec-like size clump unresolved within this survey beam, sometimes internally heated by embedded sources. Multiple gas and dust temperatures are therefore expected to be convolved within a single measurement. The correlation between the gas and dust estimates could be largely affected by the different sensitivity and weights of these mea-

surements within this beam. As result, this survey does not allow the inspection temperature structure of individual clumps. Instead, we use this analysis to explore the  $I(\text{HCN})/I(\text{HNC})$  intensity variations in different Galactic environments in a statistical manner.

We display the comparison between the  $T_K(\text{HCN}/\text{HNC})$  and  $T_{\text{dust}}$  temperatures in all the MALT90 clumps with simultaneous HCN, HNC, and dust measurements in Figure 8c (blue dots). Despite their observational caveats, the strong temperature dependence of the HCN/HNC ratio still prevails within the MALT90 sample. Although obviously noisier than our high-resolution data, we observe a global correlation between the  $T_{\text{dust}}$  and  $T_K(\text{HCN}/\text{HNC})$  measurements (blue contours) following the same trend defined in our ISF data (red contours), particularly at  $T_K > 10$  K.

The close correspondence between the predicted  $T_K(\text{HCN}/\text{HNC})$  gas temperatures and the observed  $T_{\text{dust}}$  dust measurements confirms the validity of the HCN/HNC line ratio as proxy of the gas temperatures beyond the ISF. The good agreement between these independent observables in regions such as Orion B (Fig. 8b) highlights the good performance of the proposed  $I(\text{HCN})/I(\text{HNC})$  line ratio as proxy of the gas kinetic temperatures at cloud scales. Moreover, the similar correlation observed in the MALT90 sample allow us to extend these local results towards different environments across the Milky Way. These results denote this newly proposed  $I(\text{HCN})/I(\text{HNC})$  line ratio as a reliable and robust estimate for the gas kinetic temperatures of the molecular ISM.

## 5. Discussion

### 5.1. HCN vs. HNC emission properties as function of temperature

The advent of broad band receivers has popularized the use of simultaneous HCN and HNC observations in a broad range of astrophysical studies. Variations on the observed the HCN/HNC intensity ratio are employed as indicator of the evolutionary stage of high-mass star-forming regions in the Milky Way (Jin et al. 2015). Large HCN/HNC intensity ratios are also observed in Seyfert (Pérez-Beaupuits et al. 2007) and starburst galaxies (Bemis & Wilson 2019). Systematic changes of this ratio are also observed between the central and disk regions of nearby galaxies (Jiménez-Donaire et al. 2019). At smaller scales, significant changes on the distribution and ratio of these two isomers have been reported from planetary nebulae to (Bublitz et al. 2019) to proto-planetary disks (Graninger et al. 2015). The robustness of results derived from our Orion observations suggest that these intensity variations may be related to changes in the gas kinetic temperatures.

We explored the influence of temperature on the observed HCN and HNC intensities in Figure 10. We display the individual HCN (top panel) and HNC (bottom panel) integrated intensities normalized by the local extinction measurements derived using *Herschel* observations (Lombardi et al. 2014) as function of the gas kinetic temperature ( $T_K(\text{HCN}/\text{HNC})$ ) for all positions along the ISF outside the ONC. The use of this extinction normalization (aka specific intensity) allows to isolate the enhanced abundance and temperature effects on the observed line intensities from their similar expected increase as function of column density.

As seen in Fig. 10, both specific HCN and HNC intensities systematically increase at higher gas kinetic temperatures  $T_K$ . However, the comparison of their individual temperature



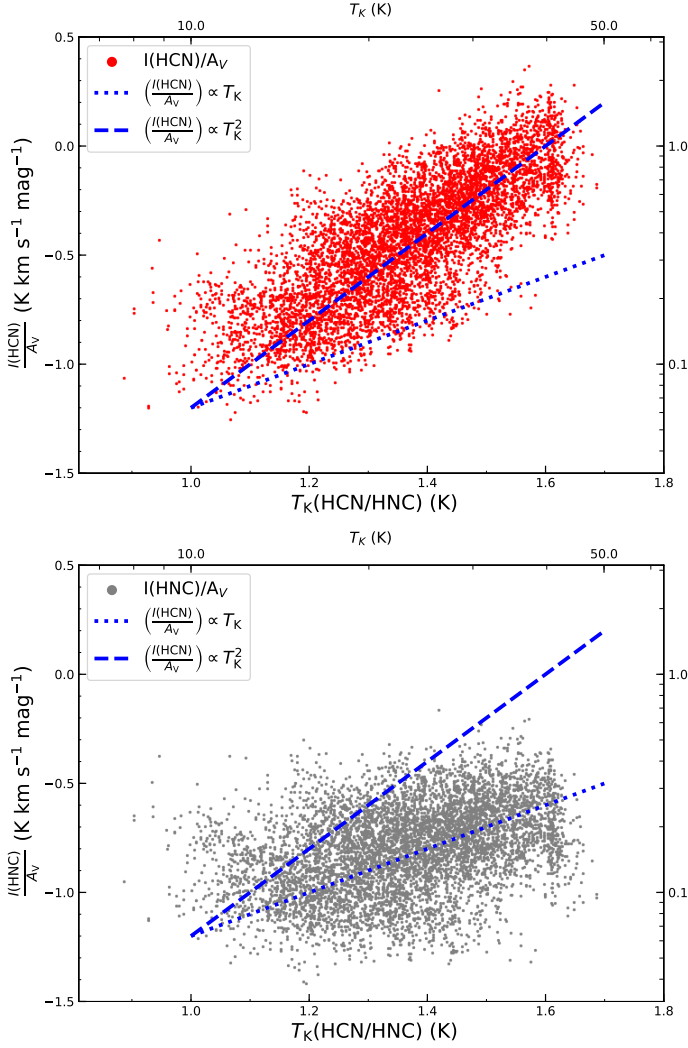


**Fig. 10.** Specific HCN (top) and HNC (bottom) intensities normalized by column density (i.e.,  $I(X)/A_V$ ) as function of the  $T_K(\text{HCN}/\text{HNC})$  gas temperatures for all positions in our ISF maps with  $I(\text{HCN})$ ,  $I(\text{HNC}) \geq 1.0 \text{ K km s}^{-1}$  outside the ONC, that is, with  $I(\text{H41}\alpha) \leq 1.0 \text{ K km s}^{-1}$ . For comparison, linear (blue dotted line) and quadratic (blue dashed line) variations of the normalized line intensities with temperature are indicated in all subpanels.

dependence shows clear differences between these two molecular tracers. HNC (bottom panel) grows linearly with temperature ( $\propto T_K$ ; blue dotted line). Much steeper, HCN (top panel) shows a quadratic dependence with the gas kinetic temperature (i.e.,  $\propto T_K^2$ ; blue dashed line). The strong temperature dependence observed in HCN produces changes of more than an order of magnitude in the intensity of this latter tracer per unit of column density within the range of temperatures considered in this work.

The different behaviours of the observed HCN and HNC emission properties shown in Fig. 10 can be explained by the combination of excitation and chemical effects. Both observed HCN and HNC intensities are enhanced by the increasing excitation conditions at higher temperatures (linear dependence). In addition to it, the observed HCN intensities are boosted (quadratic dependence) by the increasing production and abundance of this isomer in lukewarm conditions above  $> 15 \text{ K}$  (see Sect. 3.3).

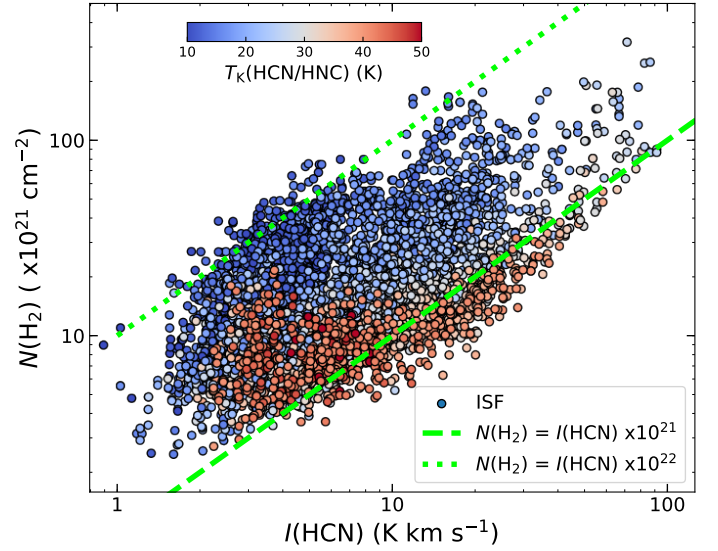


**Fig. 11.** Correlation between the observed total HCN intensities  $I(\text{HCN})$  and the total gas column density  $N(\text{H}_2)$  for all positions in our maps, colour-coded by their gas kinetic temperature (see scale bar on the top left corner). Note the large spread in our data (up to 1 dex) for a given column density  $N(\text{H}_2)$  or intensity  $I(\text{HCN})$  value.

## 5.2. On the interpretation of HCN observations in extragalactic studies

The magnitude of the above temperature variations significantly alters the correlation between the observed HCN intensities  $I(\text{HCN})$  and total gas column densities  $N(\text{H}_2)$ , that is, the so-called X-factor for HCN. Under normal excitation conditions, the HCN intensities are expected to grow with  $N(\text{H}_2)$  due to the intrinsic correlation between  $N(\text{H}_2)$  and  $n(\text{H}_2)$  (Bisbas et al. 2019). However, the resulting intensity at a given column density can strongly depend on the gas temperature (see Sect. 5.1). We quantified this effect in Figure 11 by comparing these two observables assuming a standard  $N(\text{H}_2)/A_V = 0.93 \times 10^{21} \text{ cm}^{-2} \text{ mag}^{-1}$  conversion (Bohlin et al. 1978). To illustrate its temperature dependence, each of our observations is colour-coded according to its corresponding  $T_K(\text{HCN}/\text{HNC})$  value. At low gas temperatures, the reported  $N(\text{H}_2)$  describes an almost linear relationship with the  $I(\text{HCN})$  intensities (e.g.,  $N(\text{H}_2)[\text{cm}^{-2}] \sim I(\text{HCN})[\text{K km s}^{-1}] \times 10^{22}$  at 10 K, see dotted line). However, this correlation is systematically shifted towards higher  $I(\text{HCN})$  values at increasing gas temperatures (e.g.,  $N(\text{H}_2)[\text{cm}^{-2}] \sim I(\text{HCN})[\text{K km s}^{-1}] \times 10^{21}$  at 40 K, see dashed line). As a result, each  $I(\text{HCN})$  intensity value represents a more than a factor of 5 in range of column densities. Similarly, a fixed  $N(\text{H}_2)$  column shows almost a 1 dex variation in intensity depending on the intrinsic gas temperature (see color coded temperatures in this figure).

Although less prominent, the reported temperature enhancements of both HCN abundances (Fig. 5) and intensities (Fig. 10) also change the line emission ratio of this molecule with respect to other tracers such as CO. In Figure 12 we show the HCN (1–0) (this work) and  $^{12}\text{CO}$  (1–0) (Nakamura et al. 2012; Shimajiri et al. 2014) line ratio  $I(\text{HCN})/I(^{12}\text{CO})$  as function of total gas column density  $N(\text{H}_2)$  within our maps (see Sect. 4.3.3 for further details). As expected, we observed a gradual increase of the  $I(\text{HCN})/I(^{12}\text{CO})$  ratio with  $N(\text{H}_2)$ . However, we identify a systematic spread in both axis associated with temperature effects (see coloured points). For the majority of the positions sampled in this plot, the same  $I(\text{HCN})/I(^{12}\text{CO})$  line ratio describes a wide

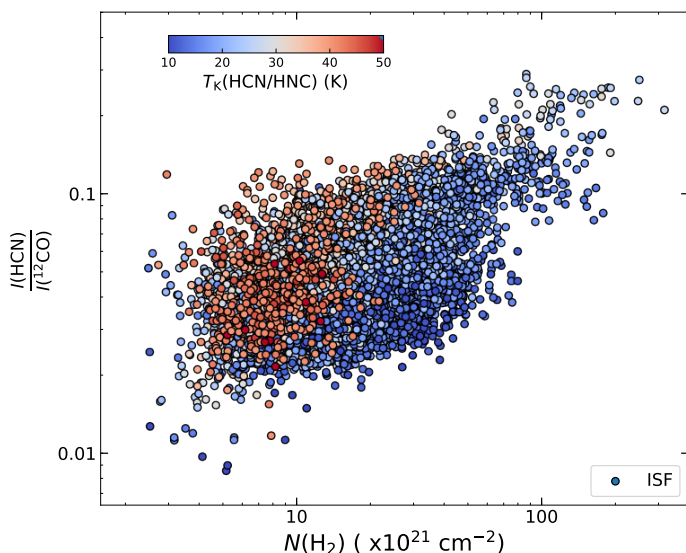


**Fig. 12.** Total gas column density  $N(\text{H}_2)$  as function of the HCN (1–0) vs  $^{12}\text{CO}$  (1–0) line intensity ratio ( $I(\text{HCN})/I(^{12}\text{CO})$ ) for all positions in our ISF maps outside the ONC with  $I(\text{H41}\alpha) \leq 1.0 \text{ K km s}^{-1}$ . All points are colour-coded by the corresponding  $T_K(\text{HCN}/\text{HNC})$  value (see scale bar on the top left corner).

range of column densities and, therefore, gas masses. Similarly, a single  $N(\text{H}_2)$  value can present up to a factor of  $\sim 5$  variation in its corresponding  $I(\text{HCN})/I(^{12}\text{CO})$  line ratio largely associated to the effects of temperature on the emission properties of the HCN lines.

Our results challenge the use of HCN observations in extragalactic sources. The pioneering works by Gao & Solomon (2004a) suggest the observed HCN luminosities as (linear) indicator of the total star-formation rate from nearby spiral galaxies to the most distant Luminous (LIGs) and Ultra Luminous Infrared Galaxies (ULIGs) (see also Wu et al. 2005)<sup>9</sup>. This interpretation assumes the HCN intensities as direct measurement of the total dense ( $n(\text{H}_2) > 10^4 \text{ cm}^{-3}$  at  $A_V > 8^{\text{mag}}$ ) and star-forming gas in these extragalactic environments (i.e.,  $M_{\text{dense}} \propto I(\text{HCN})$ ; see Lada et al. 2012, for a full discussion). Contrary to it, local observations of resolved molecular clouds demonstrate that the integrated HCN (1–0) intensity at parsec scales is dominated by the contribution of more diffuse gas ( $n(\text{H}_2) < 10^3 \text{ cm}^{-3}$ ) at low column densities ( $A_V < 6^{\text{mag}}$ ) (Kauffmann et al. 2017). Recent calculations suggest that part of these enhanced HCN intensities at low extinctions could be produced by electron collisions (Goldsmith & Kauffmann 2017). The strong temperature dependence of the HCN total integrated intensities reported in our work adds another layer of complexity to this interpretation. As demonstrated by Fig. 10, the specific HCN intensity per-unit-of-column density (i.e.  $\frac{I(\text{HCN})}{A_V}$ ) produced at temperatures of  $\sim 40 \text{ K}$  exceeds by more than an order of magnitude the intensity of the same amount of gas at temperatures of  $\sim 10 \text{ K}$ . Moreover, these same temperature effects also increase the HCN emission with respect to more diffuse tracers such as CO as illus-

trated on Fig. 12. Based on these results we speculate that a non-negligible part of the HCN luminosities in these spiral, LIGs, and ULIGs galaxies could originate from the increase of the average gas temperature in these extragalactic sources. Rather than measuring the content of dense gas converted into stars, the reported HCN luminosities would then reflect the increasing impact of stellar feedback onto the surrounding molecular material in high-mass star-forming regions such as Orion. Systematic local and extragalactic observations of both HCN and HNC tracers are needed to confirm this hypothesis beyond our data.

## 6. Conclusions

In this work, we characterized the distribution and emission properties of both HCN and HNC isomers along the Integral Shape Filament (ISF) in Orion using a new set of large-scale HCN and HNC (1–0) IRAM30m maps. We compared our new IRAM30m data with ancillary GBT- $\text{NH}_3$  (Friesen et al. 2017) and *Herschel* (Lombardi et al. 2014) observations and analysed them with a new set of chemical models. This unique combination allow us to explore the use of the observed  $I(\text{HCN})/I(\text{HNC})$  intensity ratios as a new chemical gas thermometer for the molecular ISM.

The main results of this work can be summarized as follows:

1. We find a strong and systematic correlation between the observed  $I(\text{HCN})/I(\text{HNC})$  intensity ratio and the ammonia-derived gas kinetic temperatures  $T_K$  in Orion, showing increasing HCN/HNC ratios at higher gas temperatures (Sect. 3.2).
2. We describe the observed variations of the  $I(\text{HCN})/I(\text{HNC})$  intensity ratios reported in the ISF using a two-part linear function at different high- ( $T_K \geq 40 \text{ K}$ ) and low- ( $T_K < 40 \text{ K}$ ) temperatures (see Sect. 4). Easily obtained in standard millimeter line observations, this empirical parametrization allows the use of this  $I(\text{HCN})/I(\text{HNC})$  ratio as direct proxy of the gas kinetic temperatures  $T_K(\text{HCN}/\text{HNC})$ .
3. Our chemical models demonstrate that the observed  $I(\text{HCN})/I(\text{HNC})$  intensity variations are driven by similar changes in the abundance ratio  $X(\text{HCN})/X(\text{HNC})$  of these two isomers due the efficient destruction of HNC via (1)  $\text{HNC} + \text{H} \rightarrow \text{HCN} + \text{H}$  and (2)  $\text{HNC} + \text{O} \rightarrow \text{NH} + \text{CO}$  reactions operating under low energy barriers  $\Delta E_i$ . Using observational estimates and model calculations we derived values of  $\Delta E_1 = 200 \text{ K}$  (Graninger et al. 2014) and  $\Delta E_2 \sim 20 \text{ K}$  (this work) for reactions (1) and (2), respectively. Our  $\Delta E_i$  estimates reduce by approximately an order of magnitude the energy barriers predicted by classical ab-initio calculations (see Sect. 3.3).
4. We used our empirical calibration of the observed  $I(\text{HCN})/I(\text{HNC})$  intensity ratio to obtain a large-scale temperature map  $T_K(\text{HCN}/\text{HNC})$  of the entire Orion ISF (Sect. 4.2). Our temperature estimates show consistent results ( $< 5 \text{ K}$ ) with independent measurements of the dust effective temperature  $T_{\text{dust}}$  derived using *Herschel* observations (Lombardi et al. 2014). Interestingly, the bright emission of both HCN and HNC isomers across our maps allows us to obtain systematic temperature measurements within a large dynamic range of column densities ( $5^{\text{mag}} < A_V \sim 100^{\text{mag}}$ ) and temperatures ( $15 \text{ K} \leq T_K \leq 40 \text{ K}$ ). Thus, our results extend previous  $\text{NH}_3$  measurements typically restricted to  $A_V > 10^{\text{mag}}$  and provide a more complete description of the thermal structure of the diffuse material in clouds like Orion down to  $A_V$  of a few mag.

<sup>9</sup> In extragalactic observations, the integrated emission of a given molecule is typically described in terms of luminosities. Line intensities ( $I$ ) and luminosities ( $L$ ) are related by  $L = I \times A$ , where  $A$  usually defines the solid angle subtended by the solid source area (e.g., see Eqs. 1–4 in Gao, & Solomon 2004b). Although indeed different when consider individual measurements, both intensity and luminosity ratios become equivalent terms, that is,  $\frac{I(\text{HCN})}{I(\text{HNC})} = \frac{L(\text{HCN})}{L(\text{HNC})}$ , in observations of a single source and using a similar beamsizes such as our ISF maps.

5. In addition to Orion A, we find an excellent correlation between our  $T_K(\text{HCN}/\text{HNC})$  gas temperature estimates and additional *Herschel*  $T_{\text{dust}}$  dust temperature measurements in similar local (Orion B; Pety et al. 2017) and galactic (MALT90; Jackson et al. 2013) surveys (Sect. 4.4). The close correspondence between these two observables in different environments confirms the potential of the  $I(\text{HCN})/I(\text{HNC})$  intensity ratio as universal thermometer for the molecular ISM.
6. Comparisons with both gas and dust temperature estimates show that the specific intensity of HCN per unit of column density is rapidly enhanced with temperature (i.e.,  $I(\text{HCN})/A_V \propto T^2$ ) in comparison to the HNC (e.g.,  $I(\text{HNC})/A_V \propto T$ ) due the combined effect of excitation plus chemical reactions (1 & 2) between these two isomers (Sect. 5.1). These systematic variations of the HCN intensities could potentially affect the interpretation of this molecule as tracer of the dense gas content in extragalactic observations (Sect. 5.2).

**Acknowledgements.** A.H. thanks the insightful discussions with A. User and M. Tafalla. This work is part of the research programme VENI with project number 639.041.644, which is (partly) financed by the Netherlands Organisation for Scientific Research (NWO). A.H. thanks the Spanish MINECO for support under grant AYA2016-79006-P. Based on observations carried out with the IRAM30m Telescope. IRAM is supported by INSU/CNRS (France), MPG (Germany) and IGN (Spain). This research made use of APLpy, an open-source plotting package for Python (Robitaille & Bressert 2012). This research made use of the WCS tools (Mink 2006). This research made use of Astropy, a community-developed core Python package for Astronomy (Astropy Collaboration et al. 2013). This research made use of TOPCAT (Taylor 2005).

## References

- Astropy Collaboration, Robitaille, T. P., Tollerud, E. J., et al. 2013, *A&A*, 558, A33
- Bally, J., Langer, W. D., Stark, A. A., & Wilson, R. W. 1987, *ApJ*, 312, L45
- Bemis, A., & Wilson, C. D. 2019, *AJ*, 157, 131
- Bisbas, T. G., Schruha, A., & van Dishoeck, E. F. 2019, *MNRAS*, 485, 3097
- Bohlin, R. C., Savage, B. D., & Drake, J. F. 1978, *ApJ*, 224, 132
- Bosman, A. D., Walsh, C., & van Dishoeck, E. F. 2018, *A&A*, 618, A182
- Bublitz, J., Kastner, J. H., Santander-García, M., et al. 2019, *A&A*, 625, A101
- Friesen, R. K., Pineda, J. E., Rosolowsky, E., et al. 2017, *ApJ*, 843, 63
- Gao, Y., & Solomon, P. M. 2004, *ApJ*, 606, 271
- Gao, Y., & Solomon, P. M. 2004, *ApJS*, 152, 63
- Garrod, R. T., Widicus Weaver, S. L., & Herbst, E. 2008, *ApJ*, 682, 283
- Ginsburg, A., Henkel, C., Ao, Y., et al. 2016, *A&A*, 586, A50
- Goicoechea, J. R., Teyssier, D., Etzaluze, M., et al. 2015, *ApJ*, 812, 75
- Goldsmith, P. F., Langer, W. D., Ellder, J., Kollberg, E., & Irvine, W. 1981, *ApJ*, 249, 524
- Goldsmith, P. F., Irvine, W. M., Hjalmarson, A., & Ellder, J. 1986, *ApJ*, 310, 383
- Goldsmith, P. F., & Langer, W. D. 1999, *ApJ*, 517, 209
- Goldsmith, P. F. 2001, *ApJ*, 557, 736
- Goldsmith, P. F., & Kauffmann, J. 2017, *ApJ*, 841, 25
- Graninger, D. M., Herbst, E., Öberg, K. I., & Vasyunin, A. I. 2014, *ApJ*, 787, 74
- Graninger, D., Öberg, K. I., Qi, C., et al. 2015, *ApJ*, 807, L15
- Guzmán, A. E., Sanhueza, P., Contreras, Y., et al. 2015, *ApJ*, 815, 130.
- Hacar, A., Alves, J., Tafalla, M., & Goicoechea, J. R. 2017a, *A&A*, 602, L2
- Hacar, A., Tafalla, M., & Alves, J. 2017, *A&A*, 606, A123
- Hacar, A., Tafalla, M., Forbrich, J., et al. 2018, *A&A*, 610, A77
- Harju, J. 1989, *A&A*, 219, 293
- Herbst, E., Terzieva, R., & Talbi, D. 2000, *MNRAS*, 311, 869
- Hernández Vera, M., Lique, F., Dumouchel, F., Hily-Blant, P., & Faure, A. 2017, *MNRAS*, 468, 1084
- Hirota, T., Yamamoto, S., Mikami, H., & Ohishi, M. 1998, *ApJ*, 503, 717
- Ho, P. T. P., & Townes, C. H. 1983, *ARA&A*, 21, 239
- Irvine, W. M., & Schloerb, F. P. 1984, *ApJ*, 282, 516
- Jackson, J. M., Rathborne, J. M., Foster, J. B., et al. 2013, *PASA*, 30, e057
- Jiménez-Donaire, M. J., Bigiel, F., Leroy, A. K., et al. 2019, *arXiv e-prints*, arXiv:1906.08779
- Jin, M., Lee, J.-E., & Kim, K.-T. 2015, *ApJS*, 219, 2
- Johnstone, D., & Bally, J. 1999, *ApJ*, 510, L49
- Jørgensen, J. K., van der Wiel, M. H. D., Coutens, A., et al. 2016, *A&A*, 595, A117
- Kauffmann, J., Goldsmith, P. F., Melnick, G., et al. 2017, *A&A*, 605, L5
- Lada, C. J., Forbrich, J., Lombardi, M., et al. 2012, *ApJ*, 745, 190
- Larson, R. B. 1985, *MNRAS*, 214, 379
- Lombardi, M., Bouy, H., Alves, J., & Lada, C. J. 2014, *A&A*, 566, A45
- Mangum, J. G., & Wootten, A. 1993, *ApJS*, 89, 123
- Martin-Pintado, J., Rodríguez-Franco, A., & Bachiller, R. 1990, *ApJ*, 357, L49
- McElroy, D., Walsh, C., Markwick, A. J., et al. 2013, *A&A*, 550, A36
- Megeath, S. T., Gutermuth, R., Muzerolle, J., et al. 2012, *AJ*, 144, 192
- Menten, K. M., Reid, M. J., Forbrich, J., & Brunthaler, A. 2007, *A&A*, 474, 515
- Mink, D. 2006, *Astronomical Data Analysis Software and Systems XV*, 204
- Müller, H. S. P., Thorwirth, S., Roth, D. A., & Winnewisser, G. 2001, *A&A*, 370, L49
- Nakamura, F., Miura, T., Kitamura, Y., et al. 2012, *ApJ*, 746, 25
- Nishimura, A., Tokuda, K., Kimura, K., et al. 2015, *ApJS*, 216, 18
- Peng, T.-C., Wyrowski, F., Zapata, L. A., et al. 2012, *A&A*, 538, A12
- Penteado, E. M., Walsh, C., & Cuppen, H. M. 2017, *ApJ*, 844, 71
- Peñaloza, C. H., Clark, P. C., Glover, S. C. O., et al. 2018, *MNRAS*, 475, 1508
- Pérez-Beaupuits, J. P., Aalto, S., & Gerebro, H. 2007, *A&A*, 476, 177
- Peterson, D. E., & Megeath, S. T. 2008, *Handbook of Star Forming Regions*, Volume I, 4, 590
- Pety, J., Guzmán, V. V., Orkisz, J. H., et al. 2017, *A&A*, 599, A98
- Pickett, H. M., Poynter, R. L., Cohen, E. A., et al. 1998, *J. Quant. Spectr. Rad. Transf.*, 60, 883
- Robitaille, T., & Bressert, E. 2012, *Astrophysics Source Code Library*, ascl:1208.017
- Schilke, P., Walmsley, C. M., Pineau Des Forets, G., et al. 1992, *A&A*, 256, 595
- Shimajiri, Y., Kitamura, Y., Saito, M., et al. 2014, *A&A*, 564, A68
- Shirley, Y. L. 2015, *PASP*, 127, 299
- Seifried, D., Haid, S., Walch, S., et al. 2019, *arXiv e-prints*, arXiv:1906.01015
- Tang, X. D., Henkel, C., Menten, K. M., et al. 2017, *A&A*, 598, A30
- Tatematsu, K., Kandori, R., Umemoto, T., & Sekimoto, Y. 2008, *PASJ*, 60, 407
- Taylor, M. B. 2005, *Astronomical Data Analysis Software and Systems XIV*, 347, 29
- Tielens, A. G. G. M., Meixner, M. M., van der Werf, P. P., et al. 1993, *Science*, 262, 86
- Ungerechts, H., Bergin, E. A., Goldsmith, P. F., et al. 1997, *ApJ*, 482, 245
- van der Tak, F. F. S., Black, J. H., Schöier, F. L., et al. 2007, *A&A*, 468, 627
- van Dishoeck, E. F. 2018, *IAU Symposium*, 3
- Walmsley, C. M., Churchwell, E., Nash, A., et al. 1982, *ApJ*, 258, L75
- Walsh, C., Nomura, H., & van Dishoeck, E. 2015, *A&A*, 582, A88
- Wootten, A., Evans, N. J., II, Snell, R., & vanden Bout, P. 1978, *ApJ*, 225, L143
- Wu, J., Evans, N. J., Gao, Y., et al. 2005, *ApJ*, 635, L173

## Appendix A: Abundance vs. intensity ratios

To characterize the HCN and HNC variations, our analysis assumes a direct correspondence between the predicted abundance ratios of these species (i.e.,  $X(\text{HCN})/X(\text{HNC})$ ) and their reported total integrated intensity ratios in our molecular maps (i.e.,  $I(\text{HCN})/I(\text{HNC})$ ) (see Sect. 3.3). This simple equality, namely,  $X(\text{HCN})/X(\text{HNC}) = I(\text{HCN})/I(\text{HNC})$ , simplifies the otherwise dedicated conversion of each individual isomeric abundance estimate into its corresponding intensity value in our large molecular dataset ( $> 5000$  positions). While motivated by the similar excitation conditions of these two isomers (e.g., Goldsmith et al. 1986), the direct correspondence between these abundance and intensity variations can be potentially affected by distinct opacity and excitation effects. In this appendix we explore the validity and limitations of this approximation for the comparison of both simulations and observations.

We simulate the expected total integrated intensity of both HCN and HNC molecules with a series of independent radiative transfer calculations using RADEX (van der Tak et al. 2007) adopting a characteristic linewidth of  $\Delta V = 1 \text{ km s}^{-1}$  and a constant gas density of  $n(\text{H}_2) = 10^4 \text{ cm}^{-3}$  similar to our fiducial Model 4 (see Sect. 3.2). Assuming that the emission of both HCN and HNC isomers is generated from the same gas parcel, we explore different abundance ratios by comparing similar column density ratios of these two isomers, that is,  $N(\text{HCN})/N(\text{HNC}) = X(\text{HCN})/X(\text{HNC})$ . To reduce the number of free parameters, we obtained the expected intensity of HCN for different column density configurations and compare them with a prototypical HNC intensity in our cloud at different gas temperatures. In particular, we simulate the total HNC integrated intensity for a fixed column density of  $N(\text{HNC}) = 10^{14} \text{ cm}^{-2}$ , equivalent to a total gas column density of  $N(\text{H}_2) = 10^{22} \text{ cm}^{-2}$  (or  $A_V \sim 10 \text{ mag}$ ) for a typical absolute abundance of  $X(\text{HNC}) \sim 10^{-8}$  according to our chemical models (see Fig. 5). At the same time, we obtained the total HCN intensity (including all hyperfine components) for distinct column densities between  $N(\text{HCN}) = 10^{13} \text{ cm}^{-2}$  and  $10^{16} \text{ cm}^{-2}$ . Effectively, this comparison allows to explore three orders of magnitude in abundance differences with  $N(\text{HCN})/N(\text{HNC}) = X(\text{HCN})/X(\text{HNC}) = [0.1, 100]$ .

Figure A.1 (left) shows the results of our RADEX simulations for gas kinetic temperatures between  $T_K = 10 \text{ K}$  and  $70 \text{ K}$  (see coloured lines) within a range of abundance variations between  $X(\text{HCN})/X(\text{HNC}) \sim 1$  and  $20$ , in agreement to the observed intensity variations seen in Fig. 10. Overall, our models show a positive correlation between their abundance and intensity ratios driven by the increasing HCN abundance. Nevertheless, the correspondence between these two quantities changes as a function of  $X(\text{HCN})/X(\text{HNC})$ . At low abundance ratios (e.g.,  $X(\text{HCN})/X(\text{HNC}) \sim 1$ ), the observed  $I(\text{HCN})/I(\text{HNC})$  intensity ratios follow an approximately 1:1 linear variation with respect to  $X(\text{HCN})/X(\text{HNC})$  as expected in the optically thin regime (see dotted line). On the other hand, opacity and saturation effects reduce the equivalent HCN intensities producing a much shallower correlation at increasing abundance ratios (i.e.,  $X(\text{HCN})/X(\text{HNC}) > 5$ ). For a constant  $T_K$  value (e.g.,  $T_K = 10 \text{ K}$ , blue line), our RADEX models illustrate the increasing differences between the observed  $I(\text{HCN})/I(\text{HNC})$  intensity variations in comparison to their corresponding  $X(\text{HCN})/X(\text{HNC})$  abundance ratios at large  $X(\text{HCN})/X(\text{HNC})$  values.

Interestingly, the reported connection between the gas kinetic temperature and the HCN production predicted by our

chemical models (Sect. 3.2) improves the correspondence between  $X(\text{HCN})/X(\text{HNC})$  and  $L(\text{HCN})/L(\text{HNC})$ . As seen in Figure A.1 (left), for a given  $X(\text{HCN})/X(\text{HNC})$  value warmer gas temperatures present higher  $I(\text{HCN})/I(\text{HNC})$  intensity values due to the enhanced excitation and intensity of the HCN (1-0) line. As a result, increasing gas temperatures at  $X(\text{HCN})/X(\text{HNC}) > 2$  can (partially) mitigate the saturation effects of opacity producing  $I(\text{HCN})/I(\text{HNC})$  intensity values much closer to the linear dependence observed at lower  $X(\text{HCN})/X(\text{HNC})$  ratios. We illustrate these changes from the results of our Model 4 (coloured dots in Fig. A.1 left). While still departing from a perfect linearity (see grey triangles), the expected correlation between the gas temperatures and abundance ratios (solid circles) reduces the differences between the intrinsic  $X(\text{HCN})/X(\text{HNC})$  abundance variations and the observed  $I(\text{HCN})/I(\text{HNC})$  intensity variations down to  $\lesssim 0.3 \text{ dex}$  across the range of  $X(\text{HCN})/X(\text{HNC})$  values explored in this work (see dashed line).

Similar to our observational analysis (e.g., Fig. 4), in Figure A.1 (right) we display the differences between the true abundance variations ( $X(\text{HCN})/X(\text{HNC})$ ; solid lines) of Model 4 with  $1/T_K$  and the corrected intensity ratios ( $I(\text{HCN})/I(\text{HNC})$ ; dashed lines) estimated by our RADEX calculations. As illustrated by this comparison, the expected  $I(\text{HCN})/I(\text{HNC})$  values show a slightly shallower dependence with temperature in comparison to  $X(\text{HCN})/X(\text{HNC})$ . As previously shown in Fig. A.1, these differences are more prominent at low  $1/T_K$  values (i.e., high temperatures). Nonetheless, these reported minor corrections are comparable to the local scatter of our observations ( $\sim 0.2 \text{ dex}$ ) and remain much smaller than the systematic temperature variations reported in our Orion observations ( $> 1 \text{ dex}$ ; grey crosses) (see Sect. 3.3). Although not identical, our results confirm the almost direct equivalence between the  $X(\text{HCN})/X(\text{HNC})$  abundance and  $I(\text{HCN})/I(\text{HNC})$  intensity ratios within the physical conditions considered in this work. For practical purposes, we therefore assume these  $X(\text{HCN})/X(\text{HNC})$  and  $I(\text{HCN})/I(\text{HNC})$  measurements as equivalent quantities, at least in a first order approximation.

## Appendix B: Chemical models: properties, parameter space, and constraints

As demonstrated in Sect. 3.3, our chemical models successfully reproduce the observed temperature dependence of the  $I(\text{HCN})/I(\text{HNC})$  intensity ratio assuming a fiducial model with energy barriers  $\Delta E_1 = 200 \text{ K}$  and  $\Delta E_2 = 20 \text{ K}$  for reactions (1) and (2), respectively, evolutionary timescales of  $\tau = 0.5 \text{ Myr}$ , densities of  $n(\text{H}_2) = 10^4 \text{ cm}^{-3}$ , and cosmic-ray ionization rates of  $\zeta = 10^{-17} \text{ s}^{-1}$ . In this Appendix we explore the potential effects of different input parameters in our chemical models in comparison to our fiducial case. Assuming a constant  $\Delta E_1 = 200 \text{ K}$  (Graninger et al. 2014), the four panels in Fig. B.1(a-d) summarize different results of our simulations after varying each of the additional  $\Delta E_2$ ,  $\tau$ ,  $n(\text{H}_2)$ , and  $\zeta$  parameters independently. With these tests our goal is to investigate the properties and degeneracies of our models, as well as to quantify the errors in our parameter estimates. For simplicity, our comparisons assume a direct correspondence between the predicted variations on the abundance ratios in our models and the observed integrated intensities ratios, that is,  $X(\text{HCN})/X(\text{HNC}) = I(\text{HCN})/I(\text{HNC})$  (see Appendix A).

Figure B.1a shows the effects of different energy barriers  $\Delta E_2$  between  $10 \text{ K}$  and  $25 \text{ K}$ . Changes in  $\Delta E_2$  are directly translated into different slopes and offsets on the expected



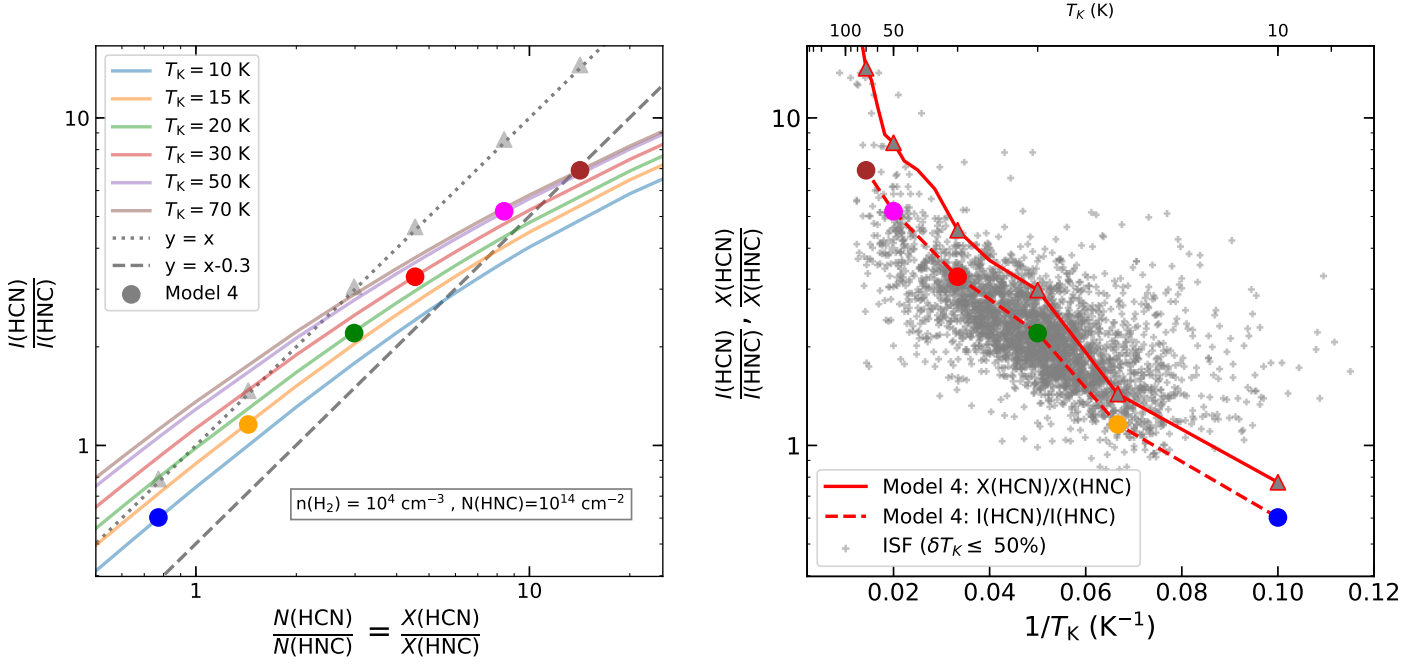


**Fig. A.1.** Comparison between the HCN vs HNC intensity ratio ( $L(\text{HCN})/L(\text{HNC})$ ) as function of the abundance ratio ( $X(\text{HCN})/X(\text{HNC})$ ) for different gas kinetic temperatures ( $T_K$ ). **(Left)** Luminosity variations for  $N(\text{HCN})/N(\text{HNC}) = X(\text{HCN})/X(\text{HNC}) = [0.1, 100]$  for gas temperatures between 10 and 70 K (coloured lines) calculated using RADEX assuming  $n(\text{H}_2) = 10^4 \text{ cm}^{-3}$  and  $N(\text{HNC}) = 10^{14} \text{ cm}^{-2}$  (see text). Linear variations are indicated by dotted ( $y=x$ ) and dashed ( $y=x-0.3$  dex) lines, respectively. The abundance and intensity ratios expected for our Model 4 are indicated by solid circles coloured according to their corresponding temperature. **(Right)** Differences between the predicted  $X(\text{HCN})/X(\text{HNC})$  (solid line) and  $L(\text{HCN})/L(\text{HNC})$  (dashed line) values for Model 4 as function of  $1/T_K$  (solid circles; similar to left panel) in comparison to our Orion observations (grey crosses), similar to Fig. 5. We notice the close correspondence between these  $X(\text{HCN})/X(\text{HNC})$  and  $L(\text{HCN})/L(\text{HNC})$  measurements under the physical conditions considered in our models.

$X(\text{HCN})/X(\text{HNC})$  abundance variations in our models within the effective temperature range of reaction (2), that is, at  $T_K < 40$  K. These variations are expected due to the exponential dependence of the observed  $X(\text{HCN})/X(\text{HNC})$  with  $\Delta E_2$  (i.e.  $\propto \exp(\frac{\Delta E_2}{T_K})$ ; Sect. 3.3). In particular, lower  $\Delta E_2$  values result into shallower temperature variations of the  $X(\text{HCN})/X(\text{HNC})$  abundance ratio. From the comparison with our observational data (grey points), our fiducial model (i.e.,  $\Delta E_2 = 20$  K) presents a reasonable fit for both low- and high-temperatures simultaneously. Nonetheless, variations of  $\Delta(\Delta E_2) \pm 5$  K can not be ruled out due to the intrinsic spread of our measurements. Additional analysis, including radiative transfer calculations and opacities, are needed to better constrain the precise value of this energy barrier  $\Delta E_2$ .

We investigate the time evolution of our chemical models in Figure B.1b. We show the temperature dependence of the  $X(\text{HCN})/X(\text{HNC})$  ratio in three representative time stamps, namely,  $\tau = 0.3$  Myr,  $\tau = 0.5$  Myr, and  $\tau = 1.0$  Myr. The results of this figure illustrate the characteristic evolutionary trend of our models. Early stages of evolution ( $\tau = 0.3$  Myr; dotted line) are dominated by reaction (1) producing a fast increase of the HCN abundance at high temperatures. This rapid evolution is followed by the comparatively slower effect of reaction (2) ( $\tau = 0.5$  Myr; solid line) determining the slope of the  $X(\text{HCN})/X(\text{HNC})$  ratio at intermediate temperatures (see above). Later on ( $\tau = 1.0$  Myr; dashed line), the combination of reactions (1) and (2) reach a steady-state (or pseudo-equilibrium) in which the observed  $X(\text{HCN})/X(\text{HNC})$  dependence remains unaltered till the end of our simulations ( $\tau = 3.0$  Myr, not shown).

We explore the effects of the gas densities in our simulations in Figure B.1c. For simplicity, we show the results for the expected  $X(\text{HCN})/X(\text{HNC})$  ratios in two of our models with

$n(\text{H}_2) = 10^3 \text{ cm}^{-3}$  (blue) evaluated at  $\tau = 0.5$  Myr (blue solid line) and  $\tau = 1.0$  Myr (blue dashed line), respectively. As denoted by the comparison with our fiducial model (red solid line), lower densities result into steeper temperature dependence of the  $X(\text{HCN})/X(\text{HNC})$  ratio at similar timescales. Interestingly, the reported  $X(\text{HCN})/X(\text{HNC})$  variations for models with  $n(\text{H}_2) = 10^3 \text{ cm}^{-3}$  and  $\tau = 0.5$  Myr (blue solid line in Fig. B.1c) resemble the functional dependence observed in models with  $n(\text{H}_2) = 10^4 \text{ cm}^{-3}$  and  $\tau = 0.3$  Myr (red dotted line in Fig. B.1b). Similarly, models with  $n(\text{H}_2) = 10^3 \text{ cm}^{-3}$  and  $\tau = 1.0$  Myr (blue dashed line) are similar to those with  $n(\text{H}_2) = 10^4 \text{ cm}^{-3}$  and  $\tau = 0.5$  Myr (fiducial model; red solid line). This time delay can be understood by the dependence of reaction (2) on the amount of free atomic O. Controlled by the interaction between the number of molecules available (aka  $n(\text{H}_2)$ ) and cosmic rays (see below), larger gas densities lead to higher absolute O densities in our models speeding up the effects of reaction (2) at low temperatures.

As for the density, the increase of the cosmic ray ionization produces an enhancement of the atomic O abundances in our models, making reaction (2) to act faster at low temperatures. We illustrate the effects of cosmic rays in Figure B.1d by displaying three different combinations of  $\tau$  and  $\zeta$  values. The selected models show indistinguishable results across the entire temperature range explored in our work. As a rule of thumb, increasing ionization rates  $\zeta$  allow our chemical models to reach their steady-state (fiducial model) in shorter timescales  $\tau$ , satisfying an approximate relationship of  $(\tau \times \zeta) \sim \text{const}$ .

Each of the above models considers the chemical evolution of an idealized portion of the ISM described by a single combination of  $\tau$ ,  $n(\text{H}_2)$ , and  $\zeta$  parameters. Our individual tests reveals some of the intrinsic degeneracies of our mod-

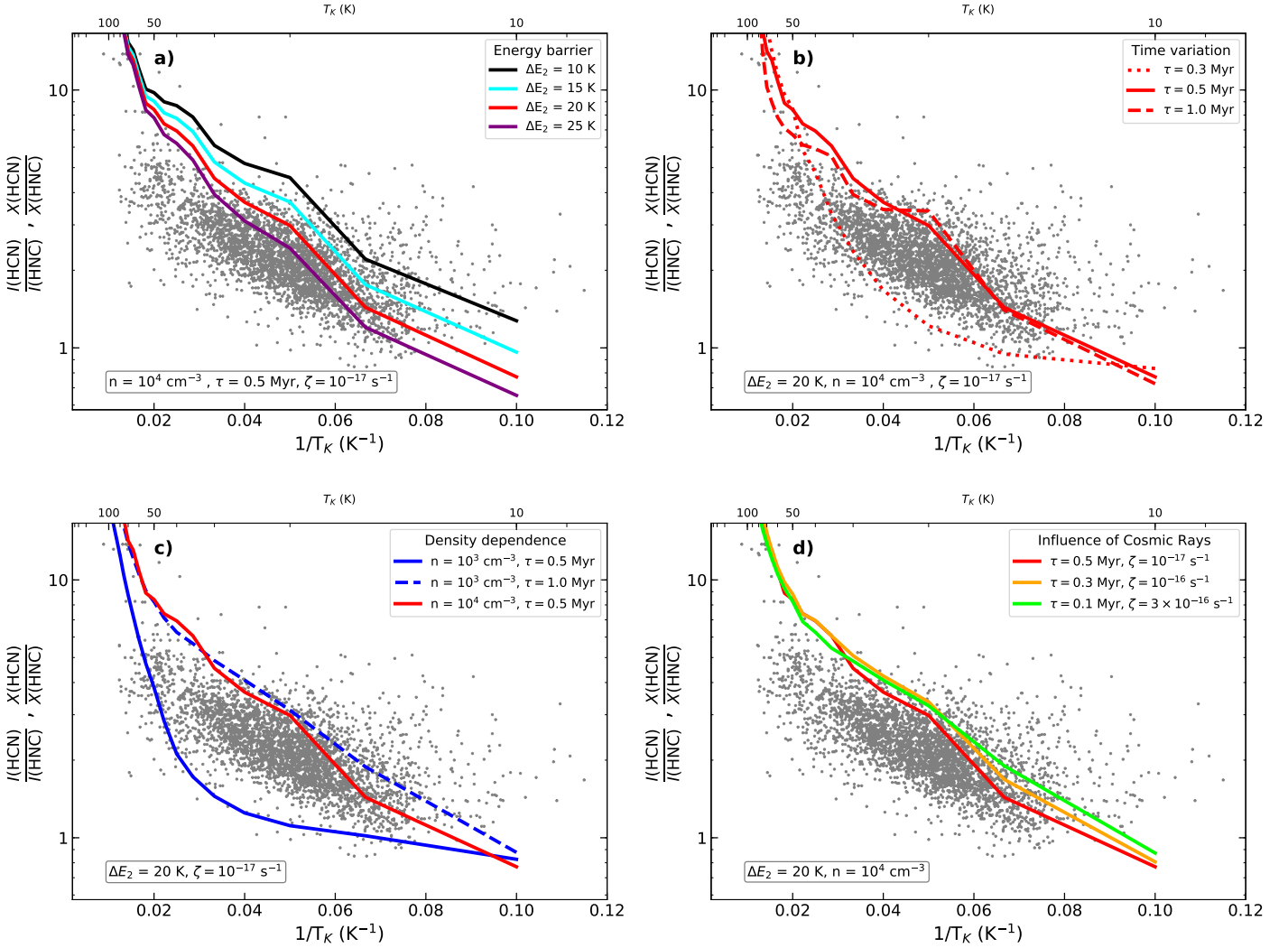


**Fig. B.1.** Predicted HCN and HNC abundances as function of  $1/T_K$  for different input parameters in our models. Data points and axes are similar to Fig. 4 b. From Left to Right and from Top to Bottom: model results for independent variations of the (a) energy barrier for reaction (2) ( $\Delta E_2$ ), (b) time evolution ( $\tau$ ), (c) gas density ( $n(\text{H}_2)$ ), and (d) cosmic-ray ionization rate ( $\zeta$ ). The input values of these models are listed and colour coded in each plot in the upper right corner of each subplot. Similarly, all fixed parameters for each of these comparisons are indicated in the lower left corner. These results are compared to our fiducial model assuming  $\Delta E_1 = 200$  K,  $\Delta E_2 = 20$  K,  $\tau = 0.5$  Myr,  $n(\text{H}_2) = 10^4 \text{ cm}^{-3}$ , and  $\zeta = 10^{-17} \text{ s}^{-1}$  (red solid line in all subplots).

els (e.g.,  $n(\text{H}_2)$  &  $\zeta$  vs.  $\tau$ ). These oversimplified simulations contrast with the definitely more complex physical conditions found in real clouds. In particular, observations in regions such as Orion undoubtedly sample a wide range of gas regions including a large variety of densities, evolutionary timescales, and radiation fields (e.g., see maps in Fig. 1). The combination of these effects is likely responsible for the spread reported in our  $I(\text{HCN})/I(\text{HNC})$  measurements. Despite all the above caveats, the predicted HCN/HNC ratios in our models show consistent results within  $\lesssim 0.4$  dex for variations of at least one order of magnitude in all  $\tau$ ,  $n(\text{H}_2)$ , and  $\zeta$  parameters. In this context, our fiducial model is meant to represent the average temperature dependence of the  $X(\text{HCN})/X(\text{HNC})$  abundance ratio under average ISM conditions. Nonetheless, additional simulations, including realistic density, chemistry, and irradiation conditions as well as detailed radiative transfer calculations (e.g., Peñaloza et al. 2018; Seifried et al. 2019) are needed to fully quantify the observed  $X(\text{HCN})/X(\text{HNC})$  abundance variations in higher detail.

Our parameter space exploration highlights the dominant role of reaction (2) at temperatures of  $T_K \lesssim 40$  K. After a

short activation period, this reaction (2) reaches a steady-state in all our models solely determined by its energy barrier  $\Delta E_2$  (Fig. B.1a). The activation timescales for reaction (2) (typically of  $\tau \sim 0.5$  Myr) are determined by the amount of atomic O available in the gas phase generated by cosmic ray ionization (see Fig. B.1c and d). Once established, however, this stable configuration remains unaltered over timescales of several Myr (Fig. B.1b). This pseudo-equilibrium, independent of the initial conditions in our models, would explain the strong correlation between  $T_K$  and  $I(\text{HCN})/I(\text{HNC})$  observed under a wide range of ISM environments in our Galaxy (see also Sect. 4.4).